International Journal of Numerical Methods for Heat & Fluid Flow

Comprehensive analysis of tetra hybrid nanofluid transport over a slender cylinder

Prabhugouda Mallanagouda Patil
Department of Mathematics, KLE Technological University, Hubli, India, and
Department of Mathematics and Applied Mathematics,
University of Johannesburg, Johannesburg, South Africa, and

Ebrahim Momoniat
Department of Mathematics and Applied Mathematics,
University of Johannesburg, Johannesburg, South Africa

Received 11 February 2026
Revised 13 May 2026
Accepted 22 May 2026

Abstract

Purpose – The purpose of this study is to investigate surface conditions that improve flow and thermal transport properties, which are essential for engineering systems, industrial processes and electronic cooling systems. Tetra hybrid nanofluids find applications in multiple industries due to their effective management of flow and heat transport.

Design/methodology/approach – A system of nondimensional partial differential equations is obtained from the original set of multidimensional, nonlinear PDEs by applying suitable non-similarity transformations. The oscillatory changes in wall velocity induced by surface roughness are illustrated as a sinusoidal waveform at the nominal mean surface.

Findings – Both graphical and tabular representations are used to provide an exhaustive analysis of key parameters related to flow dynamics and thermal performance. The rough surface of the cylinder induces sinusoidal variations in the skin friction coefficient, with the amplitude of these variations increasing with growing values of n. The rate of heat transfer through the wall in the presence of a rough surface exhibits a more pronounced oscillatory decrease along the wall length. The sinusoidal changes have a greater impact due to a periodic magnetic field (M). The present outcomes are validated through comparison with earlier results, indicating complete consistency with previous studies.

Originality/value – This research presents a numerical solution of Newtonian tetra hybrid nanofluid flow over a slender cylinder, accounting for surface roughness and a periodic magnetic field. The tetrahybrid nanofluid is composed of Ag-Au-Cu-TiO nanoparticles that enhance heat transfer due to their high thermal conductivity.

Keywords Tetrahybrid nanofluid (TeHNF), Slender cylinder, Periodic magnetic field, Surface roughness, Heat generation/absorption, Quasilinearisation, Implicit finite difference, Surface roughness

Paper type Research paper

Nomenclature

B = *Magnetic field strength*;
C_{pf} = Specific heat capacity;
C_f = Skin friction;

Funding: National Research Foundation, 150070.

International Journal of Numerical Methods for Heat & Fluid Flow
Emerald Publishing Limited
0961-5539
DOI 10.1108/HFF-02-2026-0180

Ec = *Viscous dissipation parameter*;
f = *Dimensionless stream function*;
G, F = *Temperature, and velocity profiles*;
g = *Gravitational acceleration*;
Gr = *Grashof number*;
κ = Thermal conductivity of fluid;
M = *Magnetic parameter*;
Nu = *Heat transfer rate*;
n = *Frequency parameter*;
Pr = *Prandtl number*;
Q = *Parameter of heat source (sink)*;
Q_0 = *Heat source (sink) coefficient*;
Re = *Reynolds number*;
Ri = *Mixed convection parameter*;
T = *Base fluid temperature*;
T_w = *Wall temperature*;
T_∞ = Ambient temperature; and
u, v = Components of velocities.

Greek symbols

α = Wall roughness parameter;
β_f = Volumetric expansion coefficient;
ϕ = Volume fraction of nanoparticles;
ρ_f = Fluid density;
ν_f = Kinematic viscosity of fluid;
σ_f = Electrical conductivity;
ψ = Stream function;
Ω = Frequency;
ϖ = Sphericity;
ε = Ratio of velocity parameter; and
η_∞ = Edge of the boundary layer.

Subscripts

f = *Base fluid*;
∞ = Away from the boundary layer;
w = *Wall condition*;
ξ, η = Derivatives w.r.t. these variables; and
tehnf = tetrahybrid *nanofluids*.

1. Introduction

Modern fluid dynamics research has focused on nanofluid flow, which is characterised by the formation of composite materials with exceptional thermal properties through the dispersion of tiny particles in a base fluid. When you add nanoparticles, which are usually oxides or metals, to a fluid, they significantly change how heat flows through it. Nanofluids have recently garnered considerable attention across several domains owing to their remarkable characteristics and versatile applications. Nanofluid is a suspension that contains nanoparticles that are mixed with a base fluid, which can be water, ethylene glycol or another similar liquid. Changes to the underlying fluid's properties improve several behaviour markers, including viscosity and thermal conductivity. Nanofluids (NFs) usually have sizes between 1 and 100 nanometres.

Adding nanoparticles to the base fluid significantly improves the nanocomposite's thermal efficiency, viscosity and visual properties. According to Animasaun *et al.* (2022), adding nanoparticles (NPs) to lubricating fluids may improve their lubrication performance, thereby reducing friction and slowing wear and tear on machine parts. This could extend equipment lifespans and reduce maintenance expenses in the industrial and automotive production industries. It is essential to understand that putting NPs into the bloodstream has significant effects. Enhanced pharmaceutical administration, personalised therapy, and advanced imaging and diagnostics can yield biomarkers with greater sensitivity. Utilising these capabilities could significantly improve personalised medicine, increase treatment efficacy, and facilitate a deeper understanding of the complexities of the vascular system.

Choi (1995) developed a model that clarifies the thermodynamic properties of nanoparticle suspensions, known as nanofluids. This model provides a reliable method for predicting the effective thermal conductivity of nanofluids, accounting for the nanoparticles' volume fraction. Since the field's inception, there has been extensive research on the dynamics of nanofluids. This endeavour has led to extensive theoretical and empirical research in this area. Grosan and Pop (2011) conducted a quantitative study of the steady, axisymmetric mixed convection flow and heat transfer around a submerged vertical cylinder in a nanofluid. This work considered specific external flow and surface-temperature conditions. By employing nanofluids, Trimbitas *et al.* (2011) effectively replicated the heat transfer and flow in a mixed convection process through a vertical needle with a movable wall at varying temperatures. To investigate how the solid volume fraction of the fluid affects heat transfer, numerical solutions of similarity equations are used with water as the base fluid and copper nanoparticles. An investigation into the steady flow and thermal transfer properties of a micropolar fluid containing nanoparticles around a vertical cylinder was conducted by Rehman and Nadeem (2012). Patil *et al.* (2019) examined the influence of surface roughness on the flow dynamics around a moving thin cylinder in the context of mixed-convection nanoliquid flow. Mkhatshwa et al. (2020) studied the flow, heat, and mass transport properties of a silver-water nanofluid near a thin vertical cylinder. The study examined the following phenomena: thermodiffusion, chemical reactions, Hall effects, and diffusion-thermal effects. In a Darcy–Brinkman medium with a tiny concave surface, Alghamdi *et al.* (2021) studied Casson simultaneous flows of nanofluids based on sodium alginate using a single-phase approach. The flow of a Williamson nanofluid around a vertical thin cylinder was examined by Farooq *et al.* (2023) in connection with WU's slip, activation energy, bioconvection and motile microorganisms. The analysis also considers thermophoresis, mass flow, thermal radiation, Brownian motion, and Cattaneo–Christov heat conduction. Patil and Benawadi (2024) examined the oxytactic bioconvection of a Casson–Williamson nanofluid as it passed through a narrow, rough cylinder. In this work, we investigated the nanoparticle's properties using the two-phase Buongiorno model.

In comparison to conventional nanofluids, a hybrid nanofluid has been developed, anticipated to exhibit improved heat transfer capabilities, enhanced rheological behaviour, and thermophysical properties. A hybrid nanofluid is better than regular nanofluids because it has two different types of nanoparticles evenly spread throughout a base fluid. Hybrid nanofluids have attracted considerable interest for examining the effects of diverse nanocomposites in various heat transfer applications, such as heat exchangers, heat sinks, solar collectors, boiling processes and micro power generation systems. Waini *et al.* (2019) examined steady mixed convection hybrid nanofluid flow on a vertical thin needle with a defined surface heat flux. Patil *et al.* (2022) examined a vertically orientated thin cylinder in motion experiencing hybrid nanofluid mixed convection and evaluated both homogeneous and heterogeneous processes. The investigation was based on the differences in diffusivity between chemical species and the

numerical solutions obtained from the nonsimilar approach. Patil and Kulkarni (2021) examined the mixed convective flow of an Ag-TiO□/water hybrid nanofluid across a thin cylinder under the influence of an external magnetic field. Aladdin *et al.* (2021) examined the two-dimensional stability of a hybrid nanofluid (Al□O□ and Cu) on a slender horizontal needle, accounting for hydromagnetic effects and slip conditions. Patil and Benawadi (2022) examined the influence of nanoparticle morphology on fluid and thermal dynamics throughout a slender cylinder with a non-uniform surface. The study, however, incorporated the effects of magnetohydrodynamics (MHD) and convective boundary conditions. This research assessed the effective viscosity and thermal conductivity of the hybrid nanoliquid using the Hamilton-Crosser model. Samat *et al.* (2024) did a numerical study of how suction moves hybrid carbon nanotubes through a thin vertical needle. The thin needle is inserted into hybrid nanofluids composed of both single- and multi-walled carbon nanotubes and water. The distinctive thermal conductivity characteristics of binary nanoparticle fluids have expanded their use across various fields. Adding more nanoparticles to nanoliquids might improve their ability to transfer heat compared to regular binary hybrid nanofluids. More nanoparticles might be added to the nanofluids. Because of this, liquids containing three different types of nanoparticles are adequate heat transfer fluids. That is why these liquids are called ternary nanofluids. Patil and Shankar (2024) examined the flow properties of ternary mixed convective Eyring-Powell nanofluids over a narrow cylinder, highlighting the effects of nonlinear thermal radiation and entropy in their analysis. We prepared a ternary nanofluid by mixing iron oxide nanoparticles with single- and multi-walled carbon nanotubes in water.

Goud *et al.* (2022) investigated the thermal fluctuation in a dovetail fin under fully saturated circumstances, employing a ternary hybrid nanofluid (ZnFe□O□ + MnZnFe□O□ + NiZnFe□O□) in H□O. This study examined fluctuations in temperature and humidity ratio as the principal factors influencing heat and mass transport, respectively. Hussein *et al.* (2025) conduct a thorough numerical and statistical analysis of ternary hybrid nanofluid flow over a permeable moving surface. This study examines how wall suction, magnetic field strength and Joule heating affect the matter. The ternary hybrid nanofluid comprising Al□O□, Cu and TiO□ nanoparticles exhibited improved thermal and flow properties when mixed with water. The main governing factors have a significant effect on performance.

Tehnfs, or tetra-hybrid nanofluids, are a novel kind of nanofluid. This cutting-edge nanofluid design keeps four different types of nanoparticles suspended in a contaminant-free fluid. This study was initiated because there is a growing need for improved thermal performance in industrial applications. This desire is the driving factor behind this innovation. To enhance the functionality of existing nanofluids, scientists have developed TeHNFs with even better thermal properties. Efforts to improve the thermal properties of hybrid nanofluids (HNFs) followed these groundbreaking studies, resulting in the development of TeHNFs. Four separate types of solid nanoparticles work together in this innovative mixture. The unique combination of nanoparticles in TeHNFs makes them very attractive in the biomedical field. These nanofluids' enhanced thermal properties enable controlled release of therapeutic substances, making them highly promising for targeted drug delivery. More than that, they can be used to treat hyperthermic cancer. TeHNFs can elevate the temperature of cancer cells while minimising damage to healthy tissue. TeHNFs are essential for advancing imaging technologies by enhancing contrast agents and improving diagnostic accuracy. Nanofluids have several potential applications, including tissue engineering, where they can improve the properties of scaffold materials and accelerate cell proliferation. Overall, TeHNFs are flexible and can be used to enhance many areas of medicine, such as imaging, diagnosis and treatment. These materials can be used in a wide range of medical settings, such as regenerative medicine, intravenous fluids, hyperthermia

therapeutic devices, thermal and ultrasound contrast agents, and more. Amudhini and De (2024) show that the thermo-diffusion effects have a significant impact on the MHD unsteady flow of a TeHNF made up of Al□O□, Cu, SiO□ and TiO□ in water inside a non-Darcy porous stretched cylinder. In addition, the characteristics of activation energy, heat output and chemical reaction are incorporated into the computation. Our understanding of how nanofluids could increase heat and mass transfer in a wide variety of contexts, including solar collectors, chemical reactors, enhanced cooling systems and medical devices, has expanded as a result of this research. Paul and Das (2024) examined the electro-pumping design of Phan-Thien-Tanner (PTT) blood flow, employing tetra-hybrid nanoparticles within a ciliated artery channel while accounting for entropy generation. The study investigated the influence of cilia on the arterial wall in relation to the postulated pumping process. Guedri *et al*. (2025) investigated the thermal performance of a TeHNF comprising Ag, TiO□, GO and Co/EG as it flows through a porous medium. There is also an external magnetic field at the same time. The simultaneous analysis of the thermal properties of hybrid, trihybrid and tetrahybrid nanofluids is enabled by incorporating viscous dissipation and heat-generating terms into the flow model's heat equation. Nisha and De (2025) conducted a quantitative study of a tetra-hybrid Sisko nanofluid, integrating nanoparticles with water as the base fluid, in the context of magnetohydrodynamic flow influenced by thermal radiation and heat sources. Gyrotactic microorganisms are suspended within and around a porous, vertical cone-and-plate configuration. The influence of tetrahybrid nanoparticles on the cone geometry of Sisko fluids, particularly with respect to heat generation, thermal radiation and chemical processes, has recently attracted increasing attention. The reason is that advancements in nanotechnology and heat management can benefit from the presence of tetra-nanoparticles in Sisko fluids. This model utilises a vertical cone and a plate as geometric configurations to evaluate the mass and heat transfer efficiencies of tetra-hybrid, di-hybrid and tri-hybrid nanofluids.

According to the author's understanding, there has been limited investigation into the transport of periodic MHD and a heat source (sink) in a tetra nanofluid in mixed convective flow over a slender rough-surface cylinder. This document emphasises several distinctive features of the study:

- Comparative examination between mono-, hybrid-, ternary- and tetra-nanofluid flows.
- How do the heat source and sink influence the flow properties?
- What effect does a periodic magnetic field have on the transmission of energy?
- Influence of rough surfaces on flow characteristics.
- Variations in the sphericity of nanoparticles.

2. The formulation and mathematical analysis

This study investigates the two-dimensional flow of a viscous, incompressible, combined convective tetra-hybrid nanofluid over a thin, rough-surfaced cylinder moving axially at a constant velocity. A *deterministic* approach (Chang, 1995; Pasaribu and Schipper, 2004) models surface roughness as a sine-wave pattern. The axial coordinate, z, is measured along the axis of the slender cylinder, while the radial coordinate, r, is ascertained from the cylinder's central axis. The point of entry from which the narrow cylinder emanates is referred to as 'Origin O'. Figure 1 illustrates the schematic diagram, while Figure 2 depicts the tetra nanoparticle mixture.

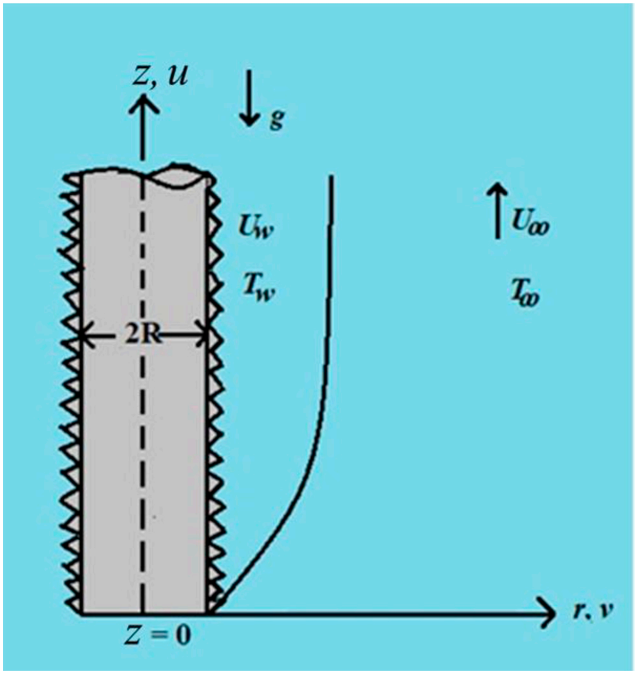

Figure 1. Flow model and coordinate system

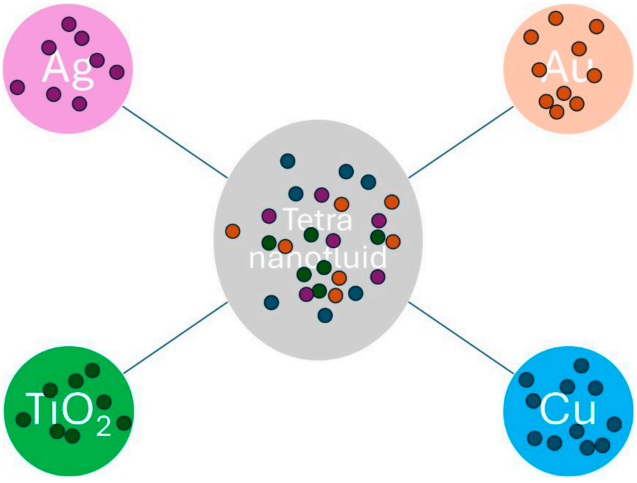

Figure 2. Mixture of Tetra nanoparticles

Further, the fluid present in the environment is moving in the axial direction at a constant velocity and contains nanoparticles. The thickness of the boundary layer is comparable to the radius of the slender cylinder. It is widely acknowledged that the temperature of the wall exceeds that of the fluid traversing its surface, as demonstrated by the phenomenon of wall cooling. Here, T represents temperature, while u and v denote the velocity components in the z and r directions, respectively. For thermal boundary layers, the Boussinesq approximation (Schlichting and Gersten, 2000) is employed, which assumes that variations in fluid density produce a body force term in the momentum equation. The following is the expression for the equation of state, where ρ^* is the reference density.

In addition, all other thermodynamic properties are constant. It is presumed that zero-dimensional nanoparticles, including *Ag* (silver), *Au* (gold), *Cu* (copper) and *TiO*□ (titanium oxide), with a size range of 1–100 nm, are incorporated into water to accomplish the necessary thermal conductivity of the resulting nanoliquid (Khan *et al.*, 2017). Both surface roughness and boundary-layer features near the surface affect the thermophysical characteristics of the thin cylinder. The following equations, which are based on the assumptions that were discussed before, are responsible for controlling the flow characteristics to ensure that mass, momentum and energy are conserved (Patil *et al.*, 2019; Patil *et al.*, 2018): The present analysis focuses on the flow over a short-radius cylinder, which has significant curvature, magnetic effects, surface roughness, and accelerated thermal diffusion due to nanofluids. The conventional flat plate boundary layer assumption ($\delta \ll R$) may not be absolutely valid. In such configurations, especially for moderate Reynolds numbers or microscale systems, the thickness of the boundary layer can be of the order of the cylinder radius, and curvature effects should be retained in the governing equations. This modelling approach is often applied in research on cylindrical and micropolar/curved surface boundary layers to achieve physical completeness rather than asymptotic simplification. We have now defined this scope more clearly and added a clarifying statement that the assumption reflects a curvature-affected boundary layer regime and not a violation of classical theory:

Mass:

$$\frac{\partial (ru)}{\partial z} + \frac{\partial (rv)}{\partial r} = 0, \tag{1}$$

Momentum:

$$v\frac{\partial u}{\partial r} + u\frac{\partial u}{\partial z} = \nu_{tehnf}\left[\frac{\partial^2 u}{\partial r^2} + \frac{1}{r}\frac{\partial u}{\partial r}\right] + \frac{(\rho\beta)_{tehnf}}{\rho_{tehnf}} g(T - T_\infty) + \frac{\sigma_{tehnf}}{\rho_{tehnf}} B^2 (u_\infty - u)\sin^2\left(\pi \frac{4}{R}\left(\frac{\nu_f z}{u_\infty}\right)^{1/2}\right) \tag{2}$$

Energy:

$$v\frac{\partial T}{\partial r} + u\frac{\partial T}{\partial z} = \frac{\kappa_{tehnf}}{(\rho C_p)_{tehnf}}\left[\frac{1}{r}\frac{\partial T}{\partial r} + \frac{\partial^2 T}{\partial r^2}\right] + \frac{Q_0}{(\rho C_p)_{tehnf}}(T - T_\infty) + \frac{\sigma_{tehnf}}{(\rho C_p)_{tehnf}} B^2 (u_\infty - u)^2 \sin^2\left(\pi \frac{4}{R}\left(\frac{\nu_f z}{u_\infty}\right)^{1/2}\right), \tag{3}$$

In accordance with the specified boundary conditions:

$$\begin{aligned} &\text{at } r = R: \quad u = u_w = u_0(1 + \alpha\sin(\Omega z)),\ v = 0,\ T = T_w, \\ &\text{as } r \to \infty: u \to \infty, \qquad\qquad T \to \infty. \end{aligned} \tag{4}$$

The physical quantities are mentioned in the nomenclature. The sinusoidal waveform $u_w = u_0(1 + \alpha\sin(\Omega z))$ represents the sinusoidal fluctuations in wall velocity produced by surface roughness at the notional mean surface at $r = R$.

Introducing nonsimilar transformations:

$$r u = \frac{\partial \psi}{\partial r},\ r v = -\frac{\partial \psi}{\partial r},\ \xi = \frac{4}{R}\left(\frac{\nu_f z}{u_\infty}\right)^{1/2},\ \eta = \left[\frac{u_\infty}{z\nu_f}\right]^{1/2}\frac{r^2 - R^2}{4R},$$

$$\psi(z, r) = f(\xi, \eta)\left[z\nu_f u_\infty\right]^{1/2} R,$$

$$F = f_\eta,\ 2u = u_\infty F,\ 2v = -\frac{R}{r}\left[\frac{\nu_f u_\infty}{z}\right]^{1/2}\{\xi f_\xi - \eta F + f\},\ G(z, r) = \frac{T - T_\infty}{T_w - T_\infty},$$

$$(1 + \xi\eta) = \frac{r^2}{R^2}. \tag{5}$$

The nonsimilar transformations delineated in (5) inherently comply with the continuity equation (1), facilitating the reformation of the momentum and energy equations (2) and (3), as well as the boundary conditions (4), into their corresponding transformed representations, as shown below:

$$\left.\begin{aligned} &C_1\left(\xi F_\eta + (1 + \xi\eta)F_{\eta\eta}\right) + C_4(\xi f_\xi + f)F_\eta - C_4\,\xi\,F\,F_\xi \\ &+ 8\,Ri\,C_2\,C_4 G + C_3 M^2 \mathrm{Re}(2 - F)\sin^2(\pi\xi) = 0, \end{aligned}\right\} \tag{6}$$

$$\left.\begin{aligned} &C_5\left[(1 + \xi\eta)G_{\eta\eta} + \xi G_\eta\right] + \mathrm{Pr}C_6[(f + \xi f_\xi)G_\eta - \xi F G_\xi] + 4\mathrm{Re}\,\mathrm{Pr}Q G \\ &+ C_3 M^2 Ec\,\mathrm{Pr}\mathrm{Re}\sin^2(\pi\xi)(2 - F)^2 = 0, \end{aligned}\right\} \tag{7}$$

And transformed boundary conditions:

$$\begin{aligned} &\text{at } \eta = 0: \quad F = 2\varepsilon\left(1 + \alpha\sin\left(n\xi^2\right)\right),\ G = 1, \\ &\text{as } \eta \to \eta_\infty: F \to 2,\ G \to 0 \end{aligned} \tag{8}$$

where $C_1 = \frac{\mu_{tehnf}}{\mu_f}$, $C_2 = \frac{\beta_{tehnf}}{\beta_f}$, $C_3 = \frac{\sigma_{tehnf}}{\sigma_f}$, $C_4 = \frac{\rho_{tehnf}}{\rho_f}$, $C_5 = \frac{\kappa_{tehnf}}{\kappa_f}$, $C_6 = \frac{(\rho C_p)_{tehnf}}{(\rho C_p)_f}$, $Ri = \frac{Gr}{\mathrm{Re}^2}$, $Gr = \frac{g\beta_f (T_w - T_\infty)z^3}{\nu_f^2}$, $\mathrm{Re} = \frac{u_\infty z}{\nu_f}$, $M^2 = \frac{B^2 \nu_f \sigma_f}{\rho_f u_\infty^2}$, $\mathrm{Pr} = \frac{(\rho C_p)_f \nu_f}{\kappa_f}$, $Q = \frac{Q_0 \nu_f}{(\rho C_p)_f u_\infty^2}$, $Ec = \frac{u_\infty^2}{Cp_f (T_w - T_\infty)}$, $n = \frac{u_\infty R^2}{16\nu_f}\Omega$, $\varepsilon = \frac{u_0}{u_\infty}$ and η_∞ be the boundary layer edge.

The following are gradient expressions in dimensionless forms:

Skin friction coefficient:

$$C_f = \frac{\mu_{tehnf}\left(\frac{\partial u}{\partial r}\right)_{r=R}}{\rho_f u_w^2},$$

$$\Rightarrow \mathrm{Re}^{1/2} Cf = \frac{\mu_{tehnf}}{4\mu_f} \frac{F_\eta(\xi,\ 0)}{\varepsilon^2\left(1+\alpha \sin n\xi^2\right)^2} \tag{9}$$

Heat transfer rate:

$$Nu = -z\frac{\kappa_{tehnf}}{\kappa_f}\frac{\left(\frac{\partial T}{\partial r}\right)_{r=R}}{(T_w - T_\infty)},$$

$$\Rightarrow NuRe^{-1/2} = -\frac{1}{2}\frac{\kappa_{tehnf}}{\kappa_f} G_\eta(\xi, 0). \tag{10}$$

3. Numerical solution

An algorithm that can solve the nonlinear coupled partial differential equations (6) and (7) with boundary conditions (8) has been developed by combining the quasilinearisation approach with the implicit finite difference method. To handle the equations appropriately, this procedure was designed. The nonlinear equations (6) and (7) are approximated by employing a methodical strategy that entails producing an iterative series of linear equations (11) and (12) and boundary conditions (8). This is done to ensure that the process is carried out correctly. In addition, this is possible because of this:

$$F_{\eta\eta}^{i+1} + A_1^i F_\eta^{i+1} + A_2^i F^{i+1} + A_3^i F_\xi^{i+1} + A_4^i G^{i+1} = A_5^i, \tag{11}$$

$$G_{\eta\eta}^{i+1} + B_1^i G_\eta^{i+1} + B_2^i G^{i+1} + B_3^i G_\xi^{i+1} + B_4^i F^{i+1} = B_5^i. \tag{12}$$

Corresponding iterative boundary conditions are the following:

$$\left.\begin{array}{lll} \eta = 0 & : F^{i+1} = 2\,\varepsilon\left(1+\alpha\sin n\xi^2\right), & G^{i+1} = 1, \\ \eta = \eta_\infty & : F^{i+1} = 2, & G^{i+1} = 0. \end{array}\right\} \tag{13}$$

In the iterative indexing scheme, the index i is designated for known functions, while index $i + 1$ is allocated to functions that remain unknown. We apply an implicit finite-difference technique (Patil *et al.*, 2013; INOUYE and Tate, 1974) to solve equations (11) and (12) subject to the boundary conditions (13). This action is undertaken to attain our objective. The finite difference scheme along the r-axis uses a central difference method, whereas the scheme along the z-axis uses a backward difference method. The equations were simplified by putting them in linear-algebraic form using a block-tridiagonal matrix. To provide solutions to the generated equations, the process was repeated at each level. To find a solution to this system, the strategy proposed by Varga (2000) was ultimately utilised. Optimisation of the numerical solution is critical, with step sizes $d\xi$ and $d\eta$, which are set to

0.01. The solution is selected in such a way that it exhibits negligible variations for η values greater than $\eta_{\max}$, *i.e.*, η_∞. The solution was determined to be sufficiently high to achieve the pertinent value at $\eta_{\max}$= 5. This guarantees that the numerical solution will eventually converge to the precise solution. The difference between the current and previous iterations serves as a criterion for convergence. Once the difference is less than or equal to 0.00001, the iteration method terminates, indicating that the solution has reached convergence:

$$\Rightarrow \max\left\{ \left|(G_\eta)_w^{(i+1)} - (G_\eta)_w^{(i)}\right|,\ \left|(F_\eta)_w^{(i+1)} - (F_\eta)_w^{(i)}\right| \right\} < 10^{-5} \tag{14}$$

Here, the coefficients appearing in equations (11) and (12) are given as follows:

$$A_1^i = \frac{C_1\xi + C_4(f+\xi f_\xi)}{C_1(1+\xi\eta)},\ A_2^i = -\frac{\left[C_4\,\xi F_\xi + C_3 M^2\,\mathrm{Re}\sin^2(\pi\xi)\right]}{C_1(1+\xi\eta)},\ A_3^i = -\frac{C_4\,\xi F}{C_1(1+\xi\eta)},$$

$$A_4^i = \frac{8\,Ri\,C_2C_4}{C_1(1+\xi\eta)},\ A_5^i = -\frac{\left[\xi F F_\xi + 2C_3M^2\,\mathrm{Re}\sin^2(\pi\xi)\right]}{C_1(1+\xi\eta)},\ B_1^i = \frac{[C_5\xi + C_6\,\mathrm{Pr}(f+\xi f_\xi)]}{C_5(1+\xi\eta)},$$

$$B_2^i = \frac{4\,\mathrm{Pr}\,\mathrm{Re}\,Q}{C_5(1+\xi\eta)},\ B_3^i = -\frac{C_6\,\mathrm{Pr}\,\xi F}{C_5(1+\xi\eta)},\ B_4^i = -\frac{\left[C_6\,\mathrm{Pr}\xi G_\xi + 2C_3M^2\,\mathrm{PrRe}\,Ec(2-F)\sin^2(\pi\xi)\right]}{C_5(1+\xi\eta)},$$

$$B_5^i = -\frac{\left[C_6\,\mathrm{Pr}\xi G_\xi F + C_3M^2\,\mathrm{PrRe}\,Ec(4-F^2)\sin^2(\pi\xi)\right]}{C_5(1+\xi\eta)}$$

4. Validation of results

The values of the gradients $\left(G_\eta(\xi,0), F_\eta(\xi,0)\right)$ are consistent with those reported by Takhar *et al.* (2000), Singh *et al.* (2008) and Roy and Anilkumar (2006), thereby ensuring the accuracy of the numerical technique. Table 1 presents strong concordance.

5. Outcomes and analysis

This section investigates the effects of various significant parameters on the profiles and gradients of flow characteristics in TeHNFs. The parameter values are considered within the specified ranges $Ri(1 \le Ri \le 10)$ $\varepsilon(0.5 \le \varepsilon \le 1.5)$, $M(0 \le M \le 2)$, $\alpha(0.0 \le \alpha \le 0.9)$, $n(1 \le n \le 75)$, $s(3 \le s \le 8.6)$, and $Q(-0.1 \le Q \le 0.1)$. However, the values of *Pr* and *Ec* are set to 7.0 and 0.1, respectively, throughout the investigation. Table 2 presents the thermophysical properties of the TeHNF, the shapes of the nanoparticles considered in this

Table 1. Thermophysical properties of tetra-hybrid nanofluid (*TeHNF*) with base fluid water [Patil *et al.*, 2024, 2025]

Physical properties	$Ag(\phi_1)$	$Au(\phi_2)$	$Cu(\phi_3)$	$TiO_2(\phi_4)$	H_2O
$\rho(kg/m^3)$	10500	19300	8960	4250	997.1
$Cp(J/kgK)$	235	129	385	686.2	4179
$k(W/mK)$	429	315	400	8.9538	0.613
$\beta(K^{-1})$	19.7×10^{-6}	16×10^{-6}	16.5×10^{-6}	8.6×10^{-6}	2.6×10^{-4}
$\sigma(\Omega m)^{-1}$	6.3×10^{7}	4.1×10^{7}	5.96×10^{7}	1×10^{-6}	5.5×10^{-6}

Table 2. The details of the nanoparticles' shapes [Timofeeva *et al.*, 2009] considered in the study

Shapes	*S*
Sphere	3
Bric	3.7
Cylinder	4.9
Platelets	5.7
Blade	8.6

study, and the corresponding physical properties of the TeHNF, respectively. At low concentrations, suspensions of *Ag*, Au, Cu and TiO_2 nanoparticles exhibit Newtonian fluid behaviour, as the particles remain uniformly dispersed and do not establish shear-dependent structures. Metallic nanofluids such as *Cu*, *Au* and *Ag* maintain Newtonian behaviour until around 0.1–1.0 vol% (Timofeeva *et al.*, 2010; Tamjid and Guenther, 2010), whereas TiO_2 nanofluids remain Newtonian until about 0.5–2.0 vol% (Pak and Cho, 1998; Kulkarni *et al.*, 2006; Chen *et al.*, 2008), provided the particles are stable and uniformly dispersed in a Newtonian base fluid. The nanoparticle volume fraction is kept at 0.05 to maintain realism in the model, ensure dispersion remains constant, and maintain Newtonian behaviour. The justification of the single-phase Newtonian model assumption for the tetra-hybrid nanofluid (Ag–Au–Cu–TiO_2/water) is mainly due to the low nanoparticle volume fractions used in the present study, where nanofluids are well known to behave as homogeneous Newtonian fluids with negligible interphase slip. For small total solid volume fractions (typically $\phi \leq 1$–3%), particle-particle interactions, agglomeration and sedimentation effects are weak, and the single-phase formulation provides results similar to the more complex multiphase models (Safaei *et al.*, 2016; Siva Shanker *et al.*, 2012; Klazly and Bognár, 2020), as shown by many experimental and numerical studies. In reality, comparison studies of single- and two-phase techniques show that for dilute concentrations, the single-phase model predicts heat transfer and flow characteristics with only small errors and is computationally efficient and physically reliable (Jouybari *et al.*, 2024).

Also, the review research papers on hybrid and multi-hybrid nanofluids always mention that dilute suspensions are stable for timeframes relevant to boundary layer and convective heat transfer assessments, provided that the nanoparticles are nanoscale and homogeneously distributed (Rashidi *et al.*, 2021; Nabwey *et al.*, 2023). Recently, single-phase Newtonian formulas have also been applied successfully to numerically investigate hybrid, tri-hybrid and tetra-hydrid nanofluids under low concentration assumptions, producing physically consistent trends and strong agreement with the literature (Amudhini and De, 2024; Gizewu and Ibrahim, 2025). Hence, the current modelling scheme is suitable for describing the macroscopic thermal and hydrodynamic behaviour of the tetra-hybrid nanofluid within the specified parametric ranges.

In the present study, the surface roughness is idealised as a periodic variation of the wall velocity, representing the effective kinematic disturbance imposed by small-scale roughness elements on the near-wall flow. This approach is widely used in laminar and transitional boundary layer investigations as a simplified way to capture the periodic momentum perturbations generated by geometrical waviness or patterned rough surfaces, without explicitly resolving the complex microgeometry. The sinusoidal form is thus a mathematical substitute for roughness-generated flow oscillations rather than a direct geometric reconstruction.

We emphasise that in the present modelling approach, the effect of surface roughness on the flow is incorporated predominantly through the momentum boundary condition, leading to a

periodic modulation of the velocity field in the vicinity of the wall. Hence, its influence on thermal transport is indirect, as it modifies the velocity field and thus convective heat transfer. Other factors such as turbulence augmentation, form drag, wake formation or roughness-driven eddy production are not included since the study is limited to the laminar boundary layer domain. We also observe that a more complete treatment, including direct geometric roughness modelling, turbulence effects or increased drag processes, would necessitate higher-order turbulence or direct numerical techniques and is outside the scope of the present work. Thus, the formulation considered should be viewed as a controlled parametric representation to explore the interaction of periodic wall-produced disturbances with magnetic modulation and nanoparticle loading rather than a thorough physical description of all roughness effects.

The volume fraction of the nanoparticle is varied from 0 to 0.05 (i.e., 0%–5%) for each type of nanoparticle, and the corresponding findings are shown in Table 3. Moreover, a constant volume fraction of 0.05 (5%) (i.e., $\phi_1 = \phi_2 = \phi_3 = \phi_4 = 5\%$ for each nanoparticle) is taken to make a direct comparison between the mono-, hybrid-, ternary- and tetrahybrid nanofluids, and the findings are shown in Table 4.

The use of the small-amplitude parameter α and the frequency parameter n are two essential parameters required to describe the surface roughness of the thin cylinder. These characteristics enable accurate simulation of the effects of roughness, which directly impact fluid flow in practical settings. In this definition, a value $\alpha = 0$ indicates a highly smooth surface, whereas higher values $(\alpha \neq 0)$ indicate progressively rougher surfaces. Cylindrical components such as heat-exchange tubes, biomedical probes, micro-cooling channels, and similar structures may experience a similar phenomenon. Roughness is mathematically represented as a sinusoidal waveform with low amplitude and high frequency to mimic these

Table 3. Physical properties of tetra-hybrid nanofluid [Paul and Das (2024)]

Physical property	Formulation
Density	$\rho_{tethnf} = (1-\phi_4)\left((1-\phi_3)\left((1-\phi_2)\left((1-\phi_1)\rho_f + \phi_1\rho_{s1}\right) + \phi_2\rho_{s2}\right) + \phi_3\rho_{s3}\right) + \phi_4\rho_{s4}$
Dynamic viscosity	$\mu_{tethnf} = \dfrac{\mu_f}{(1-\phi_1)^{2.5}(1-\phi_2)^{2.5}(1-\phi_3)^{2.5}(1-\phi_4)^{2.5}}$
Thermal conductivity	$\dfrac{k_{tethnf}}{k_f} = \begin{cases} \dfrac{k_{s4}+2k_{thnf}-2\phi_4(k_{thnf}-k_{s4})}{k_{s4}+2k_{thnf}+\phi_4(k_{thnf}-k_{s4})} \times \dfrac{k_{s3}+2k_{hnf}-2\phi_3(k_{hnf}-k_{s3})}{k_{s3}+2k_{hnf}+\phi_3(k_{hnf}-k_{s3})} \times \\ \dfrac{k_{s2}+2k_{nf}-2\phi_2(k_{nf}-k_{s3})}{k_{s2}+2k_{nf}+\phi_2(k_{nf}-k_{s3})} \times \dfrac{k_{s1}+2k_f-2\phi_1(k_f-k_{s1})}{k_{s1}+2k_f+\phi_1(k_f-k_{s1})} \end{cases}$
Heat capacity	$(\rho Cp)_{tethnf} = (1-\phi_4)\left((1-\phi_3)\left((1-\phi_2)\left((1-\phi_1)(\rho Cp)_f + \phi_1(\rho Cp)_{s1}\right) + \phi_2(\rho Cp)_{s2}\right) + \phi_3(\rho Cp)_{s3}\right) + \phi_4(\rho Cp)_{s4}$
Thermal expansion	$(\rho\beta)_{tethnf} = (1-\phi_4)\left((1-\phi_3)\left((1-\phi_2)\left((1-\phi_1)(\rho\beta)_f + \phi_1(\rho\beta)_{s1}\right) + \phi_2(\rho\beta)_{s2}\right) + \phi_3(\rho\beta)_{s3}\right) + \phi_4(\rho\beta)_{s4}$
Electrical conductivity	$\dfrac{\sigma_{tethnf}}{\sigma_f} = \begin{cases} \dfrac{\sigma_{s4}+2\sigma_{thnf}-2\phi_4(\sigma_{thnf}-\sigma_{s4})}{\sigma_{s4}+2\sigma_{thnf}+\phi_4(\sigma_{thnf}-\sigma_{s4})} \times \dfrac{\sigma_{s3}+2\sigma_{hnf}-2\phi_3(\sigma_{hnf}-\sigma_{s3})}{\sigma_{s3}+2\sigma_{hnf}+\phi_3(\sigma_{hnf}-\sigma_{s3})} \times \\ \dfrac{\sigma_{s2}+2\sigma_{nf}-2\phi_2(\sigma_{nf}-\sigma_{s3})}{\sigma_{s2}+2\sigma_{nf}+\phi_2(\sigma_{nf}-\sigma_{s3})} \times \dfrac{\sigma_{s1}+2\sigma_f-2\phi_1(\sigma_f-\sigma_{s1})}{\sigma_{s1}+2\sigma_f+\phi_1(\sigma_f-\sigma_{s1})} \end{cases}$

Table 4. Comparison of surface gradients $F_\eta(\xi, 0)$, $G_\eta(\xi, 0)$ of the current analysis with the outcomes of [Takhar *et al.* (2000)], [Singh *et al.* (2008)] and [Roy and Anilkumar (2006)] when $M = ec = 0$, $\alpha = 0$ and $n = 0$

		[Takhar *et al.* (2000)]		[Singh *et al.* (2008)]		[Roy and Anilkumar (2006)]		Current results	
ξ	*Ri*	$G_\eta(\xi, 0)$	$F_\eta(\xi, 0)$	$G_\eta(\xi, 0)$	$F_\eta(\xi, 0)$	$G_\eta(\xi, 0)$	$F_\eta(\xi, 0)$	$G_\eta(\xi, 0)$	$F_\eta(\xi, 0)$
0	0	0.5855	1.3281	0.5855	1.3280	0.5854	1.3282	0.5856	1.3279
0	1	0.8219	4.9662	0.8221	4.9662	0.8222	4.9662	0.8223	4.9663
0	2	0.9303	7.7118	0.9304	7.7119	0.9302	7.7119	0.9304	7.7119
1	0	0.8667	1.9168	0.8667	1.9168	0.8668	1.9168	0.8670	1.9169
1	1	1.0618	5.2579	1.0619	5.2578	1.0619	5.2578	1.0620	5.2580
1	2	1.1684	7.8864	1.1693	7.8862	1.1693	7.8862	1.1694	7.8863

real-world surface defects. Microtextures with periodic patterns can be generated using this process in a manner analogous to that of additive manufacturing, wear or machining. This guarantees that the model accurately portrays scenarios prevalent in technological and industrial contexts. Consequently, this is classified as a roughness profile, in accordance with ISO Standard 4287:1997, rather than a waviness profile. This attention is taken when selecting numerical values for parameters during the computation of boundary-layer profiles and gradients. As a result of the non-similarity transformation of the governing equations, the frequency parameter (n) has evolved into a combination of the surface roughness frequency (Ω) and the other physical parameters of interest. This is achieved by combining the surface roughness frequency with various physical properties.

5.1 The effects of ε and *Ri* on the temperature and velocity profiles and gradients

Figures 3–5 illustrate the effects of the mixed convection parameter, *Ri*, and the velocity ratio parameter ε on the velocity $F(\xi, \eta)$ and temperature $G(\xi, \eta)$ profiles, as well as their respective gradients $\mathrm{Re}^{1/2}Cf$ and $\mathrm{Re}^{-1/2}Nu$. The ranges selected in the present study have

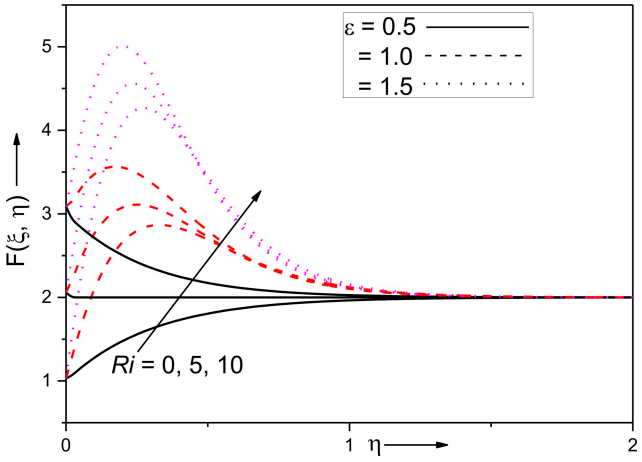

Figure 3. Variations of *Ri* and ε on $F(\xi, \eta)$

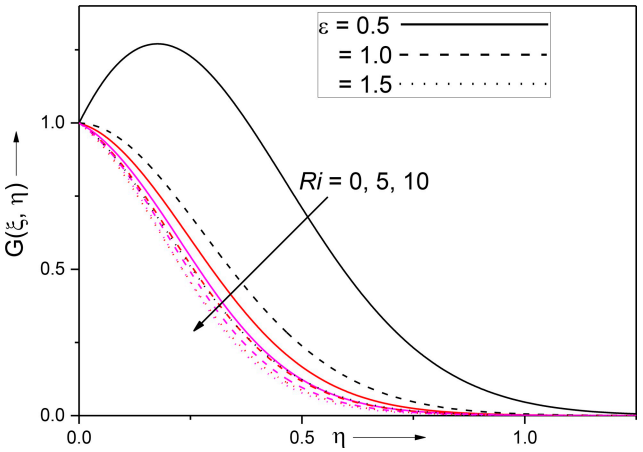

Figure 4. Variations of Ri and ε on $G(\xi,\ \eta)$

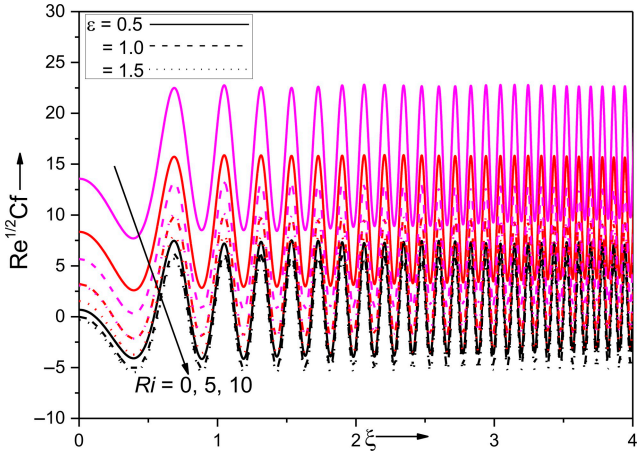

Figure 5. Variations of Ri and ε on $\mathrm{Re}^{1/2}Cf$

been purposely chosen to cover weak to strong regimes often employed in theoretical and numerical investigations so as to capture the whole parametric influence and not to reflect a single fixed operating condition. The Richardson number (Ri) is considered from 0 to 10 to span the transition from forced convection ($Ri \ll 1$) to mixed convection ($Ri \approx 1$) and buoyancy-dominated flow ($Ri > 1$). These values are often used in mixed convection over vertical or curved surfaces, microscale devices, and flows with thermal and magnetic effects, where buoyancy forces may be comparable to or larger than inertial forces. Therefore, $Ri \leq 1$ defines a physically relevant region for thermally driven systems such as cooling channels, heat exchangers and magnetically controlled flows.

The fluid's velocity (Figure 3) increases with the rising magnitudes of Ri, whereas its temperature (Figure 4) decreases. The assisting buoyancy force is augmented by an increase

in *Ri*, thereby contributing additional momentum to the fluid. This ε establishes the proportion between the wall velocity and the freestream velocity. The case of $\varepsilon < 1$ signifies that the freestream velocity predominates over the wall velocity, whereas $\varepsilon \geq 1$ implies that the wall velocity prevails over the freestream velocity. Thus, in the case of $\varepsilon < 1$ where the wall velocity is less than the freestream velocity, this results in an increase in the fluid velocity and a decrease in the boundary-layer temperature. An increase in the fluid velocity removes hotter fluid particles from the boundary layer, allowing cooler fluid particles to approach the wall. The fluid's temperature decreases as a direct consequence of this. In particular, the fluid velocity is significantly higher for $\varepsilon \geq 1$ when compared to $\varepsilon < 1$, due to the higher wall velocity which drags the fluid near it more firmly than the mainstream. Thus, the convected heat in the boundary layer results in a temperature rise, as evidenced in Figure 4. Furthermore, the effects on the velocity profile F due to are more significant compared to those due to *Ri*.

The $\mathrm{Re}^{1/2}Cf$ (Figure 5) increases along the length of the cylinder ξ in the presence of wall surface roughness. Due to the roughness of the cylinder wall surface, sinusoidal fluctuations are observed in the $\mathrm{Re}^{1/2}Cf$, and the size of these variations increases with increasing values of *Ri* while decreases as ε increases, as shown in Figure 5. Also, the effects due to ε are more prominent as compared to those due to *Ri*. However, the rate of heat transfer $\mathrm{Re}^{-1/2}Nu$ characteristics also exhibits an oscillatory nature (Figure 6). It is observed to increase significantly with increasing *Ri* and ε. Also, the effects on $\mathrm{Re}^{-1/2}Nu$ due to ε are more prominent as compared to those due to *Ri*.

5.2 Wall roughness on $Re^{1/2}Cf$

Figures 7(a)–(c) illustrate the influence of the surface roughness parameter α and the frequency parameter n on the skin-friction coefficient $\mathrm{Re}^{1/2}Cf$ along the axial coordinate of the cylinder. Figure 7(a) presents the variation of the skin-friction coefficient for different values of the roughness parameter $\alpha = 0,\ 0.01,\ 0.05$ *and* 0.1 at a fixed frequency $n = 5$, where $\alpha = 0$ corresponds to a hydraulically smooth surface. The results reveal a pronounced oscillatory behaviour of the skin-friction coefficient superimposed on an overall increasing trend along the cylinder length. This increase is physically attributed to the progressive

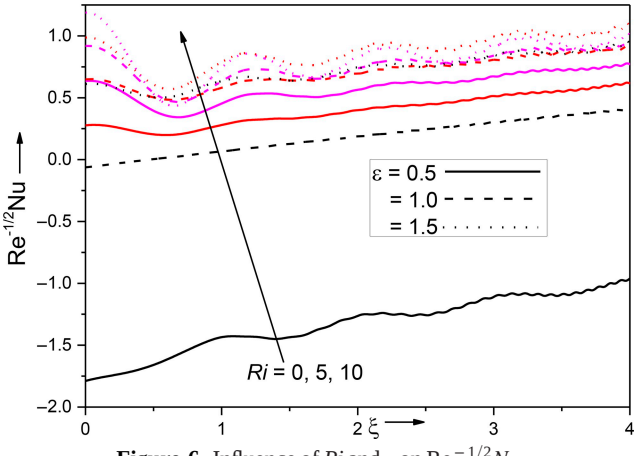

Figure 6. Influence of *Ri* and ε on $\mathrm{Re}^{-1/2}Nu$

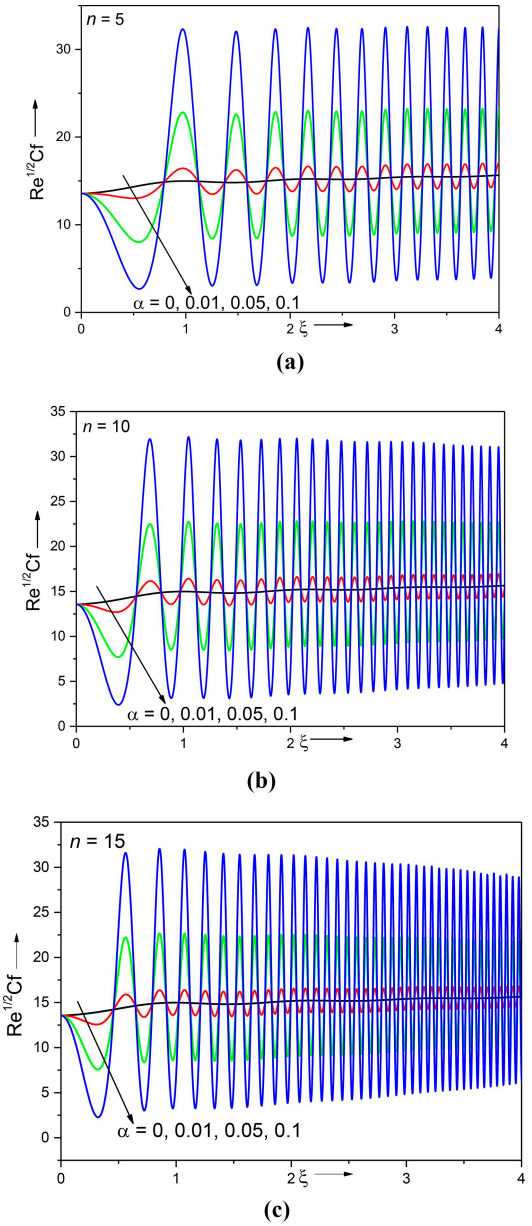

Figure 7. (a) Effects of α on $\mathrm{Re}^{1/2}Cf$ when $n = 5$, (b) Effects of α on $\mathrm{Re}^{1/2}Cf$ when $n = 10$, (c) Effects of α on $\mathrm{Re}^{1/2}Cf$ when $n = 15$

growth of the boundary layer and the accumulation of viscous shear effects downstream. The rough surface enhances momentum exchange between the fluid and the wall, thereby increasing the mean skin friction compared to the smooth configuration. From a physical perspective, surface roughness introduces periodic geometric disturbances in the form of protuberances and cavities. In the present model, these features are represented by sinusoidal waves characterised by an amplitude parameter and a frequency n. These undulations modify the near-wall velocity gradients by locally accelerating the flow over crests and decelerating it within cavities, thereby generating periodic pressure and shear variations. Consequently, sinusoidal fluctuations in the skin-friction coefficient $\mathrm{Re}^{1/2}Cf$ are observed, with increasing amplitude as the roughness frequency n increases, indicating stronger spatial modulation of wall shear stress. Figures 7(b) and (c), corresponding to $n = 10$ and $n = 15$, respectively, further demonstrate that higher frequency roughness leads to more rapid oscillations in the skin-friction coefficient. As the wavelength of the roughness decreases, the flow experiences more frequent disturbances within a given axial distance. Each cavity can temporarily trap fluid, forming local recirculation zones, while the peaks enhance local shear due to flow acceleration. This alternating mechanism intensifies the periodic variation in wall shear stress.

These findings have important implications in several real-world engineering applications. For instance, in pipeline transport systems (such as crude oil or chemical transport), internal surface roughness significantly affects pressure drop and energy consumption, as increased skin friction leads to higher pumping power requirements. In aeronautical and marine engineering, surface roughness on aircraft fuselages or ship hulls alters boundary layer behaviour, increasing drag and reducing fuel efficiency. Conversely, controlled roughness is sometimes deliberately introduced to enhance mixing and heat transfer, such as in heat exchangers and cooling systems, where rough surfaces promote turbulence and improve thermal performance. In microfluidic and biomedical devices, surface texture can influence flow resistance and fluid transport, which is critical for designing lab-on-chip systems and modelling blood flow in roughened arterial walls. Similarly, in coating and material engineering, roughness plays a key role in determining adhesion, wear and flow characteristics over surfaces. Overall, the combined effect of roughness amplitude and frequency increases the average skin-friction coefficient and introduces significant spatial oscillations, reflecting the complex relationship between viscous forces and geometrically induced flow disturbances. These insights are essential for both minimising drag in transport systems and optimising heat and mass transfer in industrial applications.

Figures 8(a)–(c) illustrate the combined effects of the frequency parameter $n$and the small amplitude parameter α on the skin-friction coefficient $\mathrm{Re}^{1/2}Cf$ along the axial coordinate ξ of the cylinder. These figures present the variation of the skin-friction coefficient for a range of frequency values $n = 1$, 5, 10, 15 and 20 corresponding to three different amplitudes of surface roughness, namely, $\alpha = 0.01$ [Figure 8(a)], $\alpha = 0.05$ [Figure 8(b)] and $\alpha = 0.1$ [Figure 8(c)]. From a physical standpoint, the skin-friction coefficient $\mathrm{Re}^{1/2}Cf$ reflects the viscous shear stress at the wall and is directly governed by the near-wall velocity gradient within the developing boundary layer. As the flow progresses along the cylinder, the boundary layer thickens and the cumulative viscous interaction between the fluid and the wall increases. This leads to an overall rise in the mean skin-friction coefficient along the axial direction, which is consistently observed in all three figures. Superimposed on this mean trend is a pronounced oscillatory behaviour induced by surface roughness. The parameter ϵrepresents the amplitude of the sinusoidal roughness elements, which physically correspond to small-scale protuberances and cavities distributed along the cylinder surface. As α increases from 0.01 to 0.1, these geometric irregularities become more prominent, causing stronger perturbations in

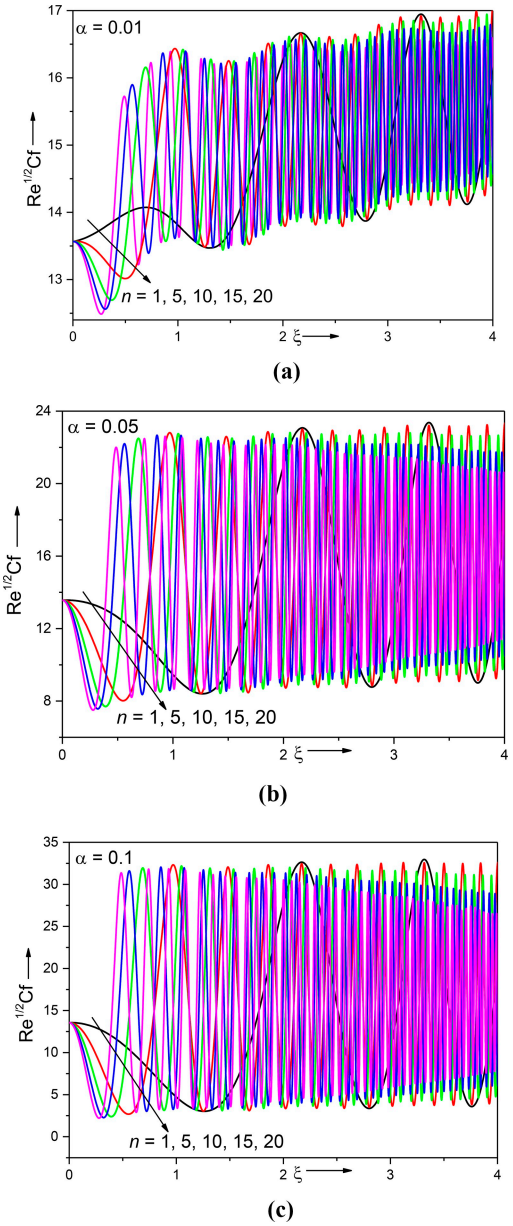

Figure 8. (a) Effects of n on $\mathrm{Re}^{1/2}Cf$ when α =0.01, (b) Variations of n on $\mathrm{Re}^{1/2}Cf$ when α = 0.05, (c) Variations of n on $\mathrm{Re}^{1/2}Cf$ when α = 0.1

the near-wall flow. This enhances the local acceleration over crests and deceleration within cavities, leading to increased fluctuations in the wall shear stress. Consequently, the amplitude of oscillations in the skin-friction coefficient $\mathrm{Re}^{1/2}Cf$ increases with α, indicating a more pronounced modulation of viscous drag due to roughness. The frequency parameter n governs the number of roughness elements per unit length, or equivalently, the wavelength of the surface undulations. As n increases, the roughness features become more closely spaced, resulting in more frequent disturbances to the boundary layer. This gives rise to rapid oscillations in the skin-friction coefficient, as seen progressively from $n = 1$ to $n = 20$. Physically, each cavity can trap a small packet of fluid, forming localised recirculation or low-velocity regions, whereas the protrusions accelerate the flow and intensify shear. The repeated alternation between these regions produces high-frequency variations in the wall shear stress distribution.

These results are highly relevant in several practical and industrial applications. For example, in pipeline transport systems, variations in internal surface roughness (due to corrosion, scaling or material degradation) directly influence frictional losses and energy requirements for pumping fluids. In aerospace and marine engineering, the roughness of surfaces such as aircraft wings or ship hulls modifies the boundary layer structure, thereby affecting drag forces and fuel efficiency. In heat transfer devices, such as compact heat exchangers, deliberately introduced roughness elements (e.g., ribs or corrugations) enhance heat transfer by increasing wall shear and promoting mixing, although this comes at the cost of higher pressure drop. Similarly, in microfluidic systems and biomedical flows, surface texture plays a crucial role in controlling flow resistance, mixing efficiency and shear-sensitive processes, such as blood flow in arteries with plaque-induced roughness. Overall, the interplay between the amplitude parameter $\epsilon$and the frequency parameter n governs the intensity and spatial variation of wall shear stress. While a larger ϵamplifies the magnitude of oscillations, higher $n$increases their frequency, together producing a complex and highly non-uniform distribution of skin friction $\mathrm{Re}^{1/2}Cf$ along the cylinder. These insights are essential for both mitigating drag in transport systems and exploiting roughness-induced effects to enhance transport processes in engineering applications.

5.3 Wall surface roughness on $Re^{-1/2}Nu$

The effects of surface roughness on $\mathrm{Re}^{-1/2}Nu$ have been analysed, and the results are portrayed in Figures 9 and 10. Remarkably, Figure 9 has plots of $\mathrm{Re}^{-1/2}Nu$ along the cylinder length ξ for the case of the variations of the roughness parameter α (small parameter) with a fixed value of frequency parameter n, while Figure 10 has that for the case of variations of frequency parameter n with a fixed value of roughness parameter α (small parameter), which is oscillatory in nature with a mean that decreases along the length of ξ. In Figures 9(a)–(c), the graphs correspond to the frequency parameter $n = 25$, 50 and 75, respectively. The chosen range of the frequency parameter (n up to 75) is also aimed at representing moderate to high oscillatory modulation of the applied magnetic field or surface roughness. Such modulation may be implemented in actual systems by using alternating current electromagnetic sources or by exploiting patterned surfaces at micro- and mesoscales. Higher values of the frequency parameter allow systematic investigation of the effects of rapid spatial or temporal fluctuations on momentum and thermal boundary layers, which is especially useful in flow control and heat transfer enhancement applications. The model does not imply that each value corresponds to a specific physical device, but it allows us to explore the limiting behaviour and sensitivity of the system.

The $\mathrm{Re}^{-1/2}Nu$ near-surface decreases and is not very effective. Away from the rough surface, i.e., $\xi > 0.6$,$\mathrm{Re}^{-1/2}Nu$ enhances significantly. For a significant value of α (*i.e.*,

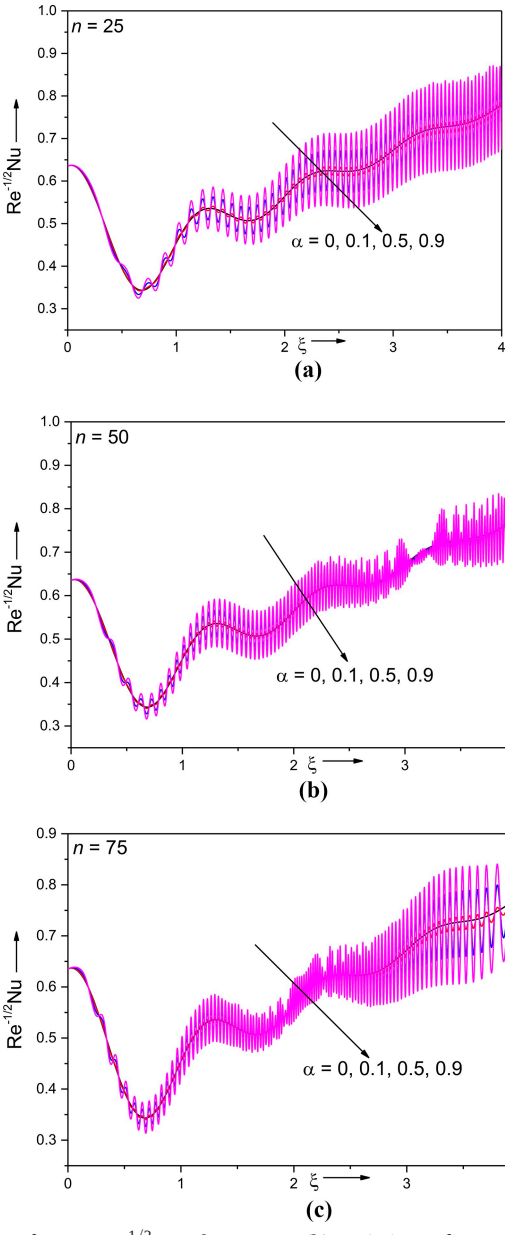

Figure 9. (a) Variations of α on $\mathrm{Re}^{-1/2}Nu$ when $n = 25$, (b) Variations of α on $\mathrm{Re}^{-1/2}Nu$ when $n = 50$, (c) Variations of α on $\mathrm{Re}^{-1/2}Nu$ when $n = 75$

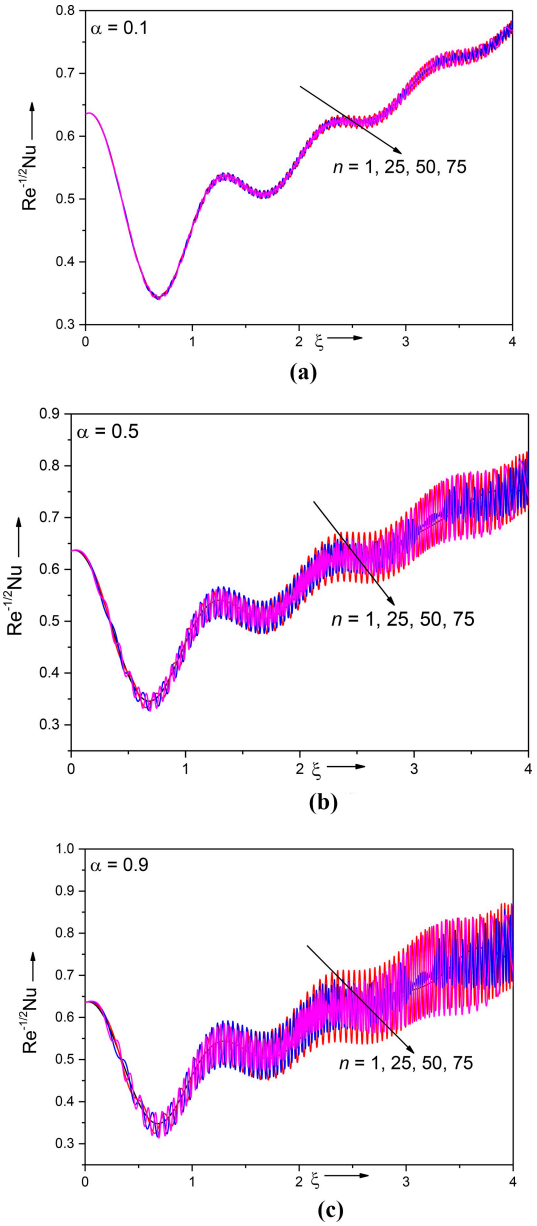

Figure 10. (a) Variations of n when on $\mathrm{Re}^{-1/2}Nu$ when α= 0.1, (b) Variations of n on $\mathrm{Re}^{-1/2}Nu$ when α= 0.5, (c) Variations of n on $\mathrm{Re}^{-1/2}Nu$ when α = 0.9

$\alpha \geq 0.5$), the disparity in wall heat transfer rates between smooth and rough surfaces is noted, increasing with the magnitude of the small parameter α. However, oscillatory behaviour is observed more clearly for $\xi > 1$ due to the synergistic influence of surface roughness and the periodic magnetic field. The more the value of n, the rougher the wall becomes, which enhances the heat transfer rate from the wall to the fluid.

On the other hand, Figures 10(a)–(c) shows plots of $\mathrm{Re}^{-1/2}Nu$ for the case of variations of frequency parameter n with a fixed value of roughness parameter α(small parameter), *i.e.*,$\alpha = 0$, 0.1, 0.5 and 0.9, respectively. It is observed that $\mathrm{Re}^{-1/2}Nu$ in the case of a rough surface, increases along the wall length occur more prominently in an oscillatory manner. When the frequency parameter increases, oscillatory behaviour becomes more pronounced in $\mathrm{Re}^{-1/2}Nu$ away from the origin of the slender cylinder surface, and consequently, the magnitude of the oscillatory behaviour rises along the length of the surface. Moreover, the magnitude of the $\mathrm{Re}^{-1/2}Nu$ is higher for the case of a higher frequency parameter n, compared to that of the lower frequency for $\alpha < 0.5$. Because of their ability to retain heat, the tetrahybrid nanoparticles in the fluid raise the liquid's temperature, thereby reducing the heat transferred from the hot wall to the fluid. The fluid cavities created by surface aspiration facilitate heat transfer from the hot wall to the surrounding cold fluid. In addition, the $\mathrm{Re}^{-1/2}Nu$ reduction throughout the length of the cylinder exhibits prominent sinusoidal oscillations. This contrasts with the situation in which a smooth surface extends along the length of the slender cylinder ξ.

5.4 Variations of M and Q on profiles and gradients of velocity and temperature

Figures 11–14 display the plots of velocity profile $F(\xi, \eta)$, temperature profile $G(\xi, \eta)$, $\mathrm{Re}^{1/2}Cf$ and $\mathrm{Re}^{-1/2}Nu$, respectively, for varying values of periodic magnetic field parameter M and heat source/sink parameter Q. The periodic magnetic field studied here is a space- or time-modulated external magnetic excitation that is physically realisable and can often be produced in practice with alternating current electromagnets, solenoid arrays or spatially distributed magnetic actuators used in electromagnetic flow and heat transfer control systems. The magnetic field is taken to be transverse to the flow direction, which is the usual configuration in the magnetohydrodynamic boundary layer analysis, as it generates a Lorentz force which opposes the fluid motion and permits effective control of the velocity

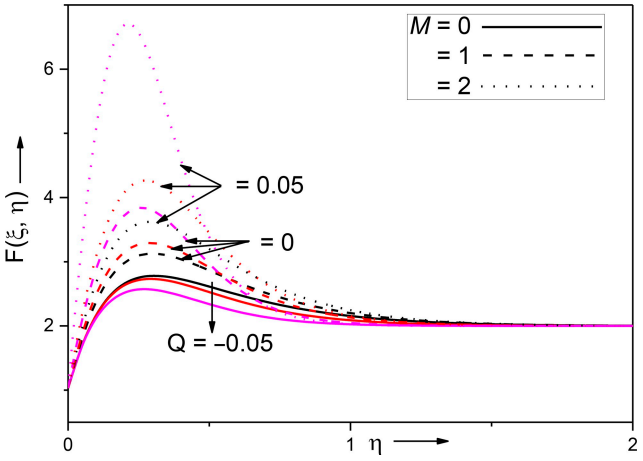

Figure 11. Effects of M and Q on $F(\xi, \eta)$

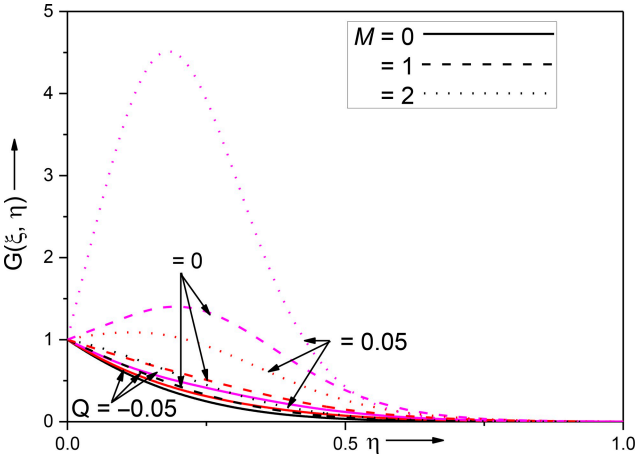

Figure 12. Variations of M and Q on $G(\xi,\ \eta)$

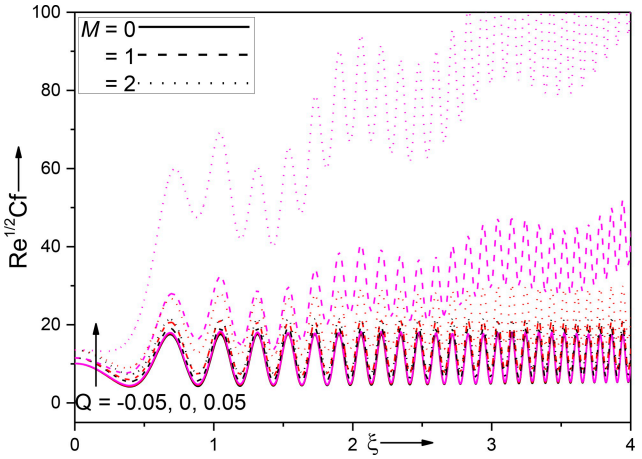

Figure 13. Effects of M and Q on $\mathrm{Re}^{1/2}Cf$

and heat fields. In the case of the magnetic field intensity, we just introduce periodicity while its orientation is fixed, which ensures physical relevance and mathematical tractability. The interaction between the oscillatory magnetic field and the surface roughness is due to the combined effect on the momentum boundary layer: the surface roughness generates spatially periodic disturbances at the wall, and the modulated magnetic field causes periodic changes in the Lorentz force inside the fluid. The coupling consequently suggests the enhancement or suppression of flow oscillations by magnetic modulation, not a rigid resonance condition. Therefore, the periodic magnetic field is used as a controllable theoretical representation to investigate the flow and heat transfer modulation in real MHD systems.

It is observed that, in general, both the profiles $F(\xi,\ \eta)$ and $G(\xi,\ \eta)$, and gradients $\mathrm{Re}^{1/2}Cf$ and $\mathrm{Re}^{-1/2}Nu$ are influenced more significantly by the magnetic field (M) than that

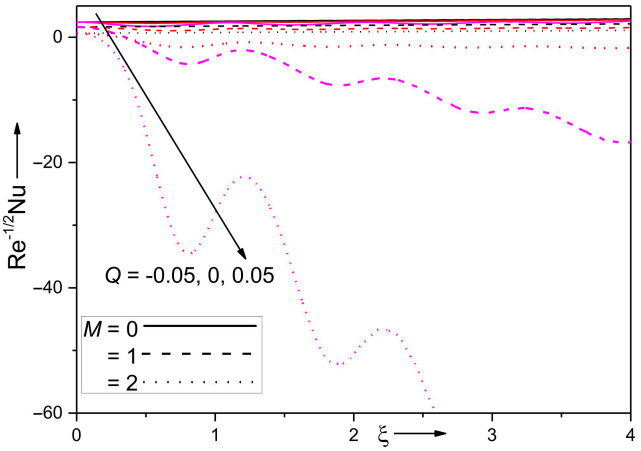

Figure 14. Effects of M and Q on $\mathrm{Re}^{-1/2}Nu$

by the heat source/sink (Q). The dramatic acceleration seen in Figure 10 is primarily attributable to the strength of the magnetic field (M) rather than the effects of the source and sink (Q). In the case of a heat source ($Q > 0$), it is observed to surpass the situation of a heat sink ($Q < 0$). The results show that the heat sink behaves oppositely to the heat source. The heat source or sink raises or lowers the buoyant force, which is responsible for this variation. Figures 11 and 12 show that when the heat source strength is substantial, the velocity and temperature profiles of the momentum and thermal boundary layers overshoot. The fluid temperature will likely decrease when heat is absorbed or when a heat sink is present ($Q < 0$). Since the effects of thermal buoyancy are diminished, the fluid's velocity is lowered. The behaviours are clearly shown in Figures 10 and 11, where the amplitude of the velocity and temperature fields decreases for ($Q < 0$).

In addition, the momentum boundary layer becomes thinner as the velocity increases. Figure 12 shows that the thermal boundary layer has similar results when a magnetic field (M) and heat generation/absorption (Q) are included.

In Figure 13, the effects of M and Q on the $\mathrm{Re}^{1/2}Cf$ are observed, which are oscillatory in nature, with their mean increasing along the wall length. The higher the M value, the higher the $\mathrm{Re}^{1/2}Cf$ value. Further, it is increased/reduced on account of a heat source ($Q > 0$)/sink ($Q < 0$), respectively. Also, the sinusoidal variations in $\mathrm{Re}^{1/2}Cf$ even in the absence of a magnetic field ($M = 0$) are owing to surface roughness. In Figure 14, it is observed that $\mathrm{Re}^{-1/2}Nu$ is impacted more significantly by the sinusoidal variations in the presence of a periodic magnetic field (M). The higher the value of M, the higher the value of $\mathrm{Re}^{-1/2}Nu$. However, in the absence of a magnetic field ($M = 0$), oscillatory behaviour is not observed. Also, $\mathrm{Re}^{-1/2}Nu$ values are increased/decreased on account of a heat sink ($Q < 0$)/source ($Q > 0$).

5.5 The effects of tetra-hybrid nanoparticles

The impact of tetrahybrid nanoparticles on $\mathrm{Re}^{1/2}Cf$ and $\mathrm{Re}^{-1/2}Nu$ is displayed in Figures 15 and 16, respectively, in comparison with mono-, hybrid- and ternary nanoparticles. In Figure 15, $\mathrm{Re}^{1/2}Cf$ is found to be increasing along the length of the wall ξ in an oscillating manner with an enhanced mean and amplitude as more nanoparticle components are added

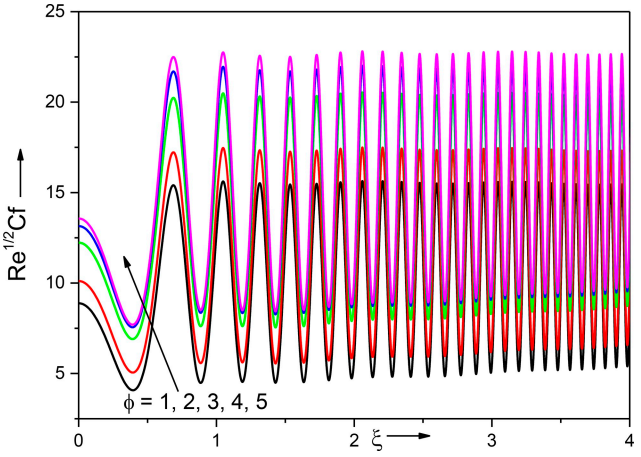

Figure 15. Impact of hybrid nanofluids on $\mathrm{Re}^{1/2}Cf$

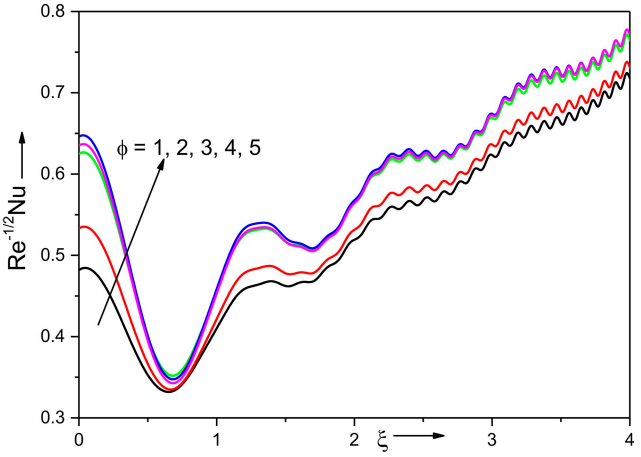

Figure 16. Impact of hybrid nanofluids on $\mathrm{Re}^{-1/2}Nu$

(labelled as 2, 3, 4 and 5) to the base fluid (labelled 1). Figure 16, $\mathrm{Re}^{-1/2}Nu$ exhibits a more pronounced oscillatory nature due to the more decisive influence of the oscillatory magnetic field. However, the mean $\mathrm{Re}^{-1/2}Nu$ increases gradually along the length of the wall ξ, and the amplitude is marginally enhanced by virtue of the additional nanoparticle components (labelled as 2, 3, 4 and 5), added to the base fluid (labelled 1). For detailed information, refer to Table 5.

The effects of nanoparticle sphericities on $\mathrm{Re}^{1/2}Cf$ and $\mathrm{Re}^{-1/2}Nu$ are depicted in Figures 17 and 18, respectively, for varying sphericities, namely, $s = 3$, 3.7, 4.9, 5.7 and 8.6. In Figure 16, the mean values of sinusoidal variations of $\mathrm{Re}^{1/2}Cf$ are enhanced and also found to increase along the length of the wall ξ significantly as the sphericity 's' increases. In Figure 17, the mean value of the sinusoidal variations of $\mathrm{Re}^{-1/2}Nu$ is also enhanced

Table 5. Description of ϕ

Label	Volume fraction ϕ			
1	$\phi_1 = 0.0$	$\phi_2 = 0.0$	$\phi_3 = 0.0$	$\phi_4 = 0.0$
2	$\phi_1 = 0.02$	$\phi_2 = 0$	$\phi_3 = 0$	$\phi_4 = 0$
3	$\phi_1 = 0.02$	$\phi_2 = 0.02$	$\phi_3 = 0$	$\phi_4 = 0$
4	$\phi_1 = 0.02$	$\phi_2 = 0.02$	$\phi_3 = 0.02$	$\phi_4 = 0$
4	$\phi_1 = 0.02$	$\phi_2 = 0.02$	$\phi_3 = 0.02$	$\phi_4 = 0.02$

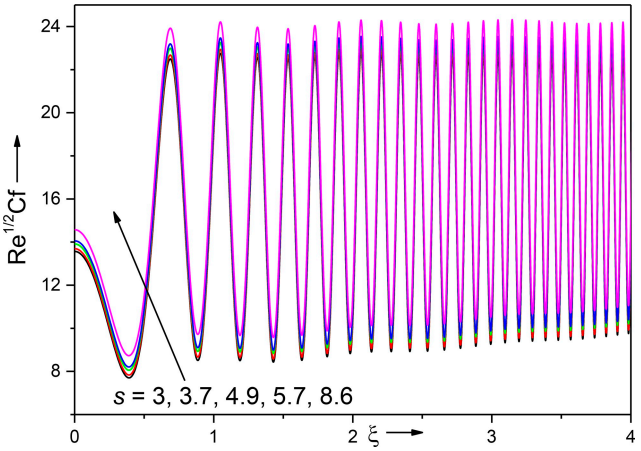

Figure 17. Impact of Sphericities on $\mathrm{Re}^{1/2}Cf$

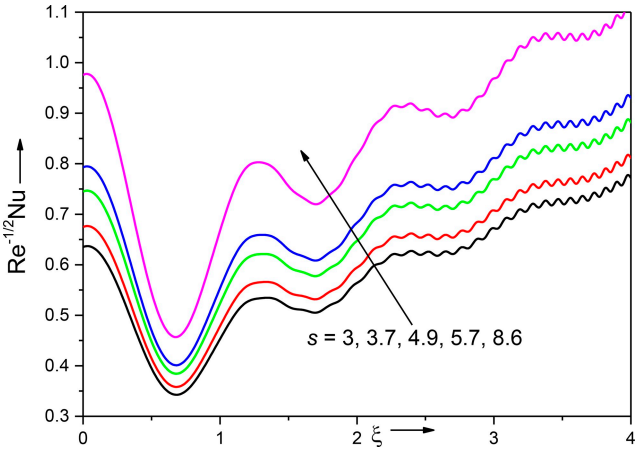

Figure 18. Impact of Sphericities on $\mathrm{Re}^{-1/2}Nu$

marginally and is also found to increase gradually along the length ξ. The effects on $\mathrm{Re}^{-1/2}Nu$ are more pronounced for higher values of sphericity s.

5.6 Effects of nanoparticle shapes on $Re^{1/2}Cf$ and $Re^{-1/2}Nu$

The sphericity of a nanoparticle's geometry is utilised to ascertain the shape factor s. The sphericity and shape factors exhibit an inverse proportionality, as indicated by the relationship $s = \frac{3}{\varpi}$ where sphericity is denoted by ϖ. The values of $\mathrm{Re}^{1/2}Cf$ increase with the rising nanoparticle volume fractions of *Ag*, *Au*, *Cu* and TiO_2, in the case of all-shaped nanoparticles, as presented in Table 6. In comparison to the other shapes of the four nanoparticles considered, skin friction is generally lower for spherical and higher for blade-shaped nanoparticles. Specifically, $TiO_2(\phi_4)$ exhibits the lowest skin friction and $Au(\phi_2)$ displays the highest skin friction, compared to the other three nanoparticles. Nevertheless, when the volume fractions of nanoparticles grow, so do the values of $\mathrm{Re}^{1/2}Cf$ for sphere, brick, cylinder, platelet and blade-shaped nanoparticles.

The enhanced skin friction is defined as $Eskf = \frac{\mathrm{Re}^{1/2}Cf(Nanofluid) - \mathrm{Re}^{1/2}Cf(Basefluid)}{\mathrm{Re}^{1/2}Cf(Basefluid)} X\,100.$

The numerical details are shown in Table 6.

The values of $\mathrm{Re}^{-1/2}Nu$ for spherical-shaped nanoparticles, as shown in Table 7, increase as the volume fraction $Ag(\phi_1)$ increases up to $\phi_1 = 0.3$ and $TiO_2(\phi_4)$ for $\phi_4 = 0.2$, then decrease $\mathrm{Re}^{-1/2}Nu$, respectively. On the other hand, $\mathrm{Re}^{-1/2}Nu$ rises when the volume fractions of nanoparticles grow, so do the values of $\mathrm{Re}^{-1/2}Nu$ spherical, brick, cylindrical, platelet and blade-shaped nanoparticles. The spherical-shaped nanoparticles exhibit an exceptionally low heat transmission rate compared to the other four shapes, and the highest heat transfer rate is displayed by blade-shaped nanoparticles. Among all four nanoparticles, $TiO_2(\phi_4)$ has the lowest heat transfer rate and $Au(\phi_2)$ demonstrates the highest heat transfer rate.

The enhanced heat transfer rate (*Ehtr*) is defined as.

$Ehtr = \frac{\mathrm{Re}^{-1/2}Nu(Nanofluid) - \mathrm{Re}^{-1/2}Nu(Basefluid)}{\mathrm{Re}^{-1/2}Nu(Basefluid)} X\,100.$ The numerical details are shown in Table 7.

The numerical results for $\mathrm{Re}^{1/2}Cf$ and *Eskf* for mono-, hybrid-, ternary- and tetra-nanofluids are summarised in Table 8, while those of $\mathrm{Re}^{-1/2}Nu$ and *Ehtr* are presented in Table 9 when compared to the base fluid. The minus sign indicates a decrease in the values relative to the base fluid. It is observed that, in general, the effect of TeHNF on gradients is more significant than that of mono-, hybrid- and ternary nanofluids. This result is of practical significance in the design of thermal control systems.

The mono-, hybrid-, ternary- and tetra-hybrid nanoparticles with a 5% volume fraction of the considered nanoparticles have been analysed for enhanced skin friction (*Eskf*), and the numerical details are given in Table 8. Suspensions of nanoparticles (*Ag*, *Au*, *Cu* and TiO_2), compared to water, with 5% volume fraction each, i.e., $\phi_1 = \phi_2 = \phi_3 = \phi_4 = 5\%$ of different shapes, namely, sphere, brick, cylinder, platelet and blade, yield enhanced skin friction (ESKF) considerably, as observed from Table 8. Among the tested nanofluids, TiO_2 exhibits the lowest skin friction (*Eskf*) of 16.59%, followed by *Cu* with 28.83%, *Ag* with 33.93% and *Au* with 52.78% for mono nanofluids of blade-shaped nanoparticles. Notably, introducing multiple nanoparticle types into hybrid nanofluids results in an additional increase in skin friction values compared to their mononanofluid counterparts. For instance, among 5% volume fractions with six possible combinations $Cu + TiO_2/H_2O$, hybrid nanofluids display the lowest enhanced skin friction (*Eskf*) of 46.43%, followed by $Ag + TiO_2/H_2O$ with 51.82%, $Ag + Cu/H_2O$ with 64.50%, $Au + TiO_2/H_2O$ with 70.86%,$Au + Cu/H_2O$ with 82.85%, and $Ag + Au/H_2O$ with 87.74%.

Table 6. $Re^{1/2}Cf$ and *e skf* for the variations of ϕ_1, ϕ_2, ϕ_3 and ϕ_4 at $\xi = 1.0$

Volume fraction of nanoparticles (5%)			$Re^{1/2}Cf$					*Eskf* (in %)		
$Ag(\phi_1)$\Shape	Sphere	Brick	Cylinder	Platelets	Blade	Sphere	Brick	Cylinder	Platelets	Blade
0.00	16.24768	16.24768	16.24768	16.24768	16.24768	–	–	–	–	–
0.01	17.19476	17.21229	17.24227	17.26165	17.33224	5.83	5.94	6.12	6.24	6.76
0.02	18.14111	18.17776	18.23997	18.28113	18.42453	11.65	11.88	12.26	12.51	13.40
0.03	19.08880	19.14622	19.24256	19.30567	19.52613	17.49	17.84	18.43	18.82	20.18
0.04	20.03831	20.11790	20.25167	20.33889	20.63786	23.33	23.82	24.64	25.18	27.02
0.05	20.99219	21.09715	21.26991	21.38174	21.76011	29.20	29.85	30.91	31.60	33.93
$Au(\phi_2)$			$Re^{1/2}Cf$					*Eskf* (in %)		
0.01	17.85195	17.87069	17.90151	17.92190	17.99655	9.87	9.99	10.18	10.35	10.76
0.02	19.41567	19.45558	19.52442	19.56877	19.72615	19.50	19.74	20.17	20.44	21.41
0.03	20.94644	21.00996	21.12084	21.19116	21.43706	28.92	29.31	29.99	30.43	31.94
0.04	22.44866	22.54089	22.69369	22.79269	23.13633	38.16	38.73	39.67	40.28	42.40
0.05	23.93039	24.05005	24.25246	24.38201	24.82332	47.28	48.02	49.27	50.06	52.78
$Cu(\phi_3)$			$Re^{1/2}Cf$					*Eskf* (in %)		
0.01	17.04686	17.06429	17.09351	17.11285	17.18221	4.92	5.03	5.21	5.32	5.75
0.02	17.84313	17.87859	17.93857	17.97817	18.11826	9.82	10.04	10.41	10.65	11.51
0.03	18.63609	18.69108	18.78427	18.84436	19.05510	14.70	15.04	15.61	15.98	17.28
0.04	19.42803	19.50295	19.62896	19.71115	19.99227	19.57	20.81	20.81	21.32	23.05
0.05	20.21835	20.31567	20.47495	20.57790	20.93233	24.44	25.04	26.02	26.65	28.83
$TiO_2(\phi_4)$			$Re^{1/2}Cf$					*Eskf* (in %)		
0.01	16.67465	16.68839	16.71158	16.72696	16.78254	2.63	2.71	2.86	2.95	3.29
0.02	17.10444	17.13203	17.17861	17.20973	17.31898	5.27	5.44	5.73	5.92	6.59
0.03	17.53866	17.58023	17.65058	17.69626	17.85742	7.95	7.95	8.63	8.92	6.76
0.04	17.97767	18.03304	18.12643	18.18701	18.39879	10.65	10.99	11.56	11.94	13.24
0.05	18.42076	18.49067	18.60755	18.68322	18.94260	13.37	13.80	14.52	14.99	16.59

Table 7. The values of $\mathrm{Re}^{-1/2}Nu$ and *Ehtr* for the variations of ϕ_1, ϕ_2, ϕ_3 and ϕ_4 at $\xi = 1.0$

Volume fraction of nanoparticles (5%)			$\mathrm{Re}^{-1/2}Nu$					*Ehtr*		
$Ag(\phi_1)$\Shape	Sphere	Brick	Cylinder	Platelets	Blade	Sphere	Brick	Cylinder	Platelets	Blade
0.00	0.40886	0.40886	0.40886	0.40886	0.40886	–	–	–	–	–
0.01	0.41670	0.42028	0.42644	0.43054	0.44518	1.92	2.79	4.30	5.30	8.88
0.02	0.42052	0.42739	0.43915	0.44687	0.47467	2.85	4.53	7.41	9.30	16.10
0.03	0.42071	0.43056	0.44729	0.45839	0.49771	2.90	5.31	9.34	12.11	21.73
0.04	0.41774	0.43025	0.45151	0.46535	0.51457	2.17	5.23	10.43	13.82	25.85
0.05	0.41191	0.42678	0.45174	0.46808	0.52572	0.75	4.38	10.49	14.48	28.58
$Au(\phi_2)$			$\mathrm{Re}^{-1/2}Nu$					*Ehtr*		
0.01	0.44082	0.44441	0.45065	0.45480	0.46961	7.82	8.69	10.22	11.24	14.86
0.02	0.46330	0.47041	0.48237	0.49031	0.51884	13.31	15.05	17.98	19.92	26.90
0.03	0.47922	0.48955	0.50681	0.51842	0.55941	17.21	19.74	23.96	26.80	36.82
0.04	0.49032	0.50354	0.52594	0.54074	0.59310	19.92	23.16	28.63	32.26	45.06
0.05	0.49748	0.51366	0.54061	0.55853	0.62116	21.67	25.63	32.22	36.61	51.92
$Cu(\phi_3)$			$\mathrm{Re}^{-1/2}Nu$					*Ehtr* (in %)		
0.01	0.42099	0.42461	0.43088	0.43504	0.44994	2.97	3.85	5.39	6.40	10.05
0.02	0.43096	0.43809	0.45024	0.45831	0.48712	5.40	7.15	10.12	12.09	19.14
0.03	0.43905	0.44955	0.46727	0.47903	0.52077	7.38	9.95	14.29	17.16	27.37
0.04	0.44560	0.45928	0.48240	0.49750	0.55140	8.99	12.33	17.99	21.68	34.86
0.05	0.45083	0.46741	0.49561	0.51412	0.57928	10.27	14.32	21.22	25.74	41.68
$TiO_2(\phi_4)$			$\mathrm{Re}^{-1/2}Nu$					*Ehtr*		
0.01	0.40870	0.41171	0.41689	0.42032	0.43275	−0.04	0.7	1.96	2.80	5.84
0.02	0.40810	0.41407	0.42426	0.43093	0.45515	−0.19	1.27	3.77	5.40	11.32
0.03	0.40704	0.41584	0.43084	0.44074	0.47626	−0.45	1.71	5.38	7.80	16.48
0.04	0.40549	0.41706	0.43670	0.44969	0.49591	−0.82	2.00	6.81	9.99	21.29
0.05	0.40351	0.41776	0.44193	0.45785	0.51446	−1.31	2.18	8.09	11.98	25.83

Table 8. Values of $Re^{1/2}Cf$ and Eskf for mono-, hybrid-, ternary-, and tetra-nanofluids when compared to the base fluid at $\xi = 1.0$

5% nanoparticles			$Re^{1/2}Cf$					*Eskf* (in %)		
Shape	Sphere	Brick	Cylinder	Platelets	Blade	Sphere	Brick	Cylinder	Platelets	Blade
Ag	20.99219	21.09715	21.26991	21.38174	21.76011	29.20	29.85	30.91	31.60	33.93
Au	23.93039	24.05005	24.25246	24.38201	24.82332	47.28	48.02	49.27	50.06	52.78
Cu	20.21835	20.31567	20.47495	20.57790	20.93233	24.44	25.04	26.02	26.65	28.83
TiO_2	18.42076	18.49067	18.60755	18.68322	18.94260	13.37	13.80	14.52	14.99	16.59
$Ag + Au$	28.31960	28.61765	29.12058	29.43519	30.50391	74.30	76.13	79.23	81.17	87.74
$Ag + Cu$	24.84002	25.09024	25.51025	25.78095	26.72663	52.88	54.42	57.00	58.67	64.50
$Ag + TiO_2$	23.15596	23.36106	23.69983	23.91924	24.66666	42.52	43.78	45.87	47.22	51.82
$Au + Cu$	27.60385	27.88701	28.35727	28.66374	29.70949	69.89	71.64	74.53	76.42	82.85
$Au + TiO_2$	26.03123	26.26253	26.65240	26.90083	27.76136	60.22	61.64	64.04	65.57	70.86
$Cu + TiO_2$	22.37751	22.56828	22.88358	23.08860	23.79152	37.73	38.90	40.84	42.10	46.43
$Ag + Au + Cu$	32.03492	32.53715	33.36322	33.89416	35.75043	97.17	100.26	105.34	108.61	120.03
$Ag + Au + TiO_2$	30.47305	30.90754	31.63557	32.10308	33.64260	87.55	90.23	94.71	97.59	107.06
$Ag + Cu + TiO_2$	27.03792	27.41031	28.02627	28.42676	29.79960	66.41	68.70	72.49	74.96	83.41
$Au + Cu + TiO_2$	29.75718	30.17106	30.86111	31.30682	32.82105	83.15	85.69	89.94	92.68	102.00
$Ag + Au + Cu + TiO_2$	34.26681	34.92581	36.01427	36.70468	39.04407	110.90	114.96	121.66	125.91	140.31

Table 9. The values of $\mathrm{Re}^{-1/2}Nu$ and *ehtr* for mono-, hybrid-, ternary-, and tetra-nanofluids when compared to the base fluid at $\xi = 1.0$

5% nanoparticles	$\mathrm{Re}^{-1/2}Nu$					*Ehtr* (in %)				
Shape	Sphere	Brick	Cylinder	Platelets	Blade	Sphere	Brick	Cylinder	Platelets	Blade
Ag	0.41191	0.42678	0.45174	0.46808	0.52572	0.75	4.38	10.49	14.48	28.58
Au	0.49748	0.51366	0.54061	0.55853	0.62116	21.67	25.63	32.22	36.61	51.92
Cu	0.45083	0.46741	0.49561	0.51412	0.57928	10.27	14.32	21.22	25.74	41.68
TiO_2	0.40351	0.41776	0.44193	0.45785	0.51446	−1.31	2.18	8.09	11.98	25.83
$Ag + Au$	0.42240	0.44877	0.49364	0.52464	0.63869	3.31	9.76	20.74	28.32	56.21
$Ag + Cu$	0.41230	0.44091	0.48998	0.52297	0.64250	0.84	7.84	19.84	27.91	57.14
$Ag + TiO_2$	0.39676	0.42443	0.47196	0.50349	0.61797	−2.96	3.81	15.43	23.14	51.14
$Au + Cu$	0.49089	0.52218	0.57660	0.61301	0.74821	20.06	27.72	41.03	49.93	83.00
$Au + TiO_2$	0.48511	0.51251	0.55942	0.59091	0.70424	18.65	25.35	36.82	44.53	72.24
$Cu + TiO_2$	0.43587	0.46685	0.52024	0.55581	0.68519	6.61	14.18	27.24	35.94	67.59
$Ag + Au + Cu$	0.39993	0.43778	0.50565	0.55285	0.72963	−2.18	7.07	23.67	35.22	78.45
$Ag + Au + TiO_2$	0.40937	0.44829	0.51544	0.56120	0.73590	0.12	9.64	26.07	37.26	79.99
$Ag + Cu + TiO_2$	0.39572	0.43726	0.50964	0.55858	0.73969	−3.21	6.95	24.65	36.62	80.92
$Au + Cu + TiO_2$	0.47409	0.51966	0.59940	0.65362	0.85732	15.95	27.10	46.06	59.86	109.69
$Ag + Au + Cu + TiO_2$	0.38819	0.43867	0.52944	0.59234	0.83550	−5.06	7.29	29.49	44.88	104.35

The suspensions of ternary hybrid nanoparticles comprise three nanoparticles among the considered nanoparticles that form four possible combinations, namely,$Ag + Cu + TiO_2/H_2O$ and $Au + Cu + TiO_2/H_2O$ with a 5% volume fraction of blade-shaped nanoparticles. These ternary nanofluids obtain enhanced skin friction (*Eskf*) of 120.03%, 107.06%, 83.41% and 102.31%, respectively. The combination $Ag + Cu + TiO_2/H_2O$ provides a lower enhanced skin friction (*Eskf*), *i.e.*, 83.41%, among the four combinations. The tetra-hybrid nanoparticles comprising all four, *Ag*, *Au*, *Cu* and TiO_2, with a 5% volume fraction of blade-shaped nanoparticles, yield 140.31%.

Overall, among the mono-, hybrid-, ternary- and tetra-hybrid-blade-shaped nanoparticles, the lowest *Eskf* values are found for TiO_2 with 16.59%, $Cu + TiO_2/H_2O$ with 46.43%, $Au + Cu + TiO_2/H_2O$ with 83.41%, and $Ag + Au + Cu + TiO_2/H_2O$ with 140.31%, respectively.

The mono-, hybrid-, ternary- and tetra-hybrid nanoparticles, each incorporated at a 5% volume fraction, were evaluated for their enhanced heat transfer performance (*Ehtr*), with the corresponding numerical results presented in Table 9. When compared to water, suspensions of nanoparticles *(Ag*, *Au*, *Cu* and TiO_2*)*, with a 5% volume fraction each, i.e. $\phi_1 = \phi_2 = \phi_3 = \phi_4 = 5\%$ of different shapes, namely, sphere, bricks, cylinders, platelets and blades, yield enhanced heat transfer rates (*Ehtr*) significantly. Among the mono nanofluids verified, Au/H_2O exhibits the highest $\mathrm{Re}^{-1/2}Nu$ of 51.92%, followed by Cu/H_2O with 41.68%, Ag/H_2O with 28.58%, and TiO_2/H_2O with 25.83%. For hybrid nanofluids with a 5% volume fraction, the six possible combinations of nanoparticles $Au + Cu/H_2O$, hybrid nanofluids display the highest enhanced heat transfer rate of 83.00%, followed by $Au + TiO_2/H_2O$ with 72.24%, $Cu + TiO_2/H_2O$ with 67.59%, $Ag + Cu/H_2O$ with 21.70%, $Ag + Au/H_2O$ with 56.21%, and $Ag + TiO_2/H_2O$ with 51.14%. When compared to base fluid, ternary hybrid nanofluids that were generated with three component combinations of the specified nanoparticles, namely *Ag*, *Au*, *Cu* and TiO_2, with a volume fraction of blade-shaped nanoparticles that was 5% were shown to be superior. These ternary nanofluids obtain enhanced heat transfer rates (*Ehtr*) of 78.45%, 79.99%, 80.92% and 109.69%, respectively. The combination $Au + Cu + TiO_2$ provides the highest enhanced heat transfer rate *Ehtr*, *i.e.*, 109.69% among the four combinations. The TeHNF, by the combination of all four nanoparticles, considered Ag + *Au* + *Cu* + TiO_2 with a 5% volume fraction for blade-shaped nanoparticles, *Ehtr* yields 104.35%. The highest values of *Ehtr* in the case of mono-, hybrid-, ternary-, and tetra-hybrid nanoparticles are *Au* with 51.92%, $Au + Cu/H_2O$ with 83.00%, $Au + Cu + TiO_2/H_2O$ with 109.69%, and Ag + *Au* + *Cu* + TiO_2 with 104.35%, respectively.

5.7 Grid discretization, grid number and grid independence test

Grid discretisation refers to the number of computational grids used in a numerical method, typically expressed in terms of grid size. Both solution accuracy and computational efficiency improve as the grid is refined, up to a best level beyond which further refinement offers negligible benefits. The computational domain, illustrated in Figure 19, is discretised using mesh sizes $\Delta\xi$ and $\Delta\eta$ along the ξ- and η- directions, respectively. Each grid point is found by an ordered pair (i, j), and the total collection of these points forms the grid number used in the numerical scheme.

To ensure numerical reliability, a grid independence test is conducted. Table 10 presents the average skin friction coefficient corresponding to grid resolutions of 100×100, 200×200, 300×300, 400×400, 500×500, 600×600, 700×700 and 800×800. The results prove that the Average skin friction coefficient stays essentially unchanged for grid sizes of 300×300 and above, showing convergence and grid insensitivity. Consequently, a uniform

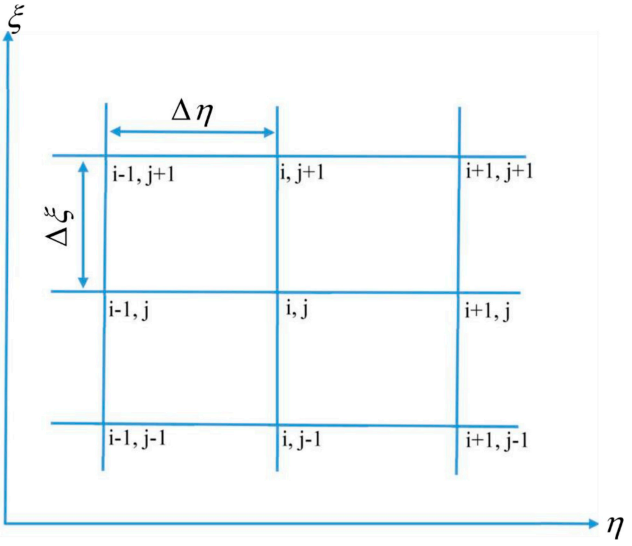

Figure 19. Grid discretization

Table 10. Grid independence test for different mesh sizes for $Ri = 5.0$, $de = 1.0$ $m = 0.5$, $Re = 10.0$, $\phi_1 = 0.02$, $\phi_2 = 0.02$, $\phi_3 = 0.02$, $\phi_4 = 0.02$, $\varepsilon = 0.5$, $M = 0.5$, $ec = 0.1$, $Q = 0.5$ and $\xi = 0.5$

Grid size	Average Skin friction coefficient ($Re^{1/2}$ Cf)
100 × 100	6.59584
200 × 200	6.77509
300 × 300	6.77553
400 × 400	6.77539
500 × 500	6.77551
600 × 600	6.77556
700 × 700	6.77549
800 × 800	6.77554

grid of 500 × 500, with mesh spacings of 0.01 along and normal to the surface, is considered sufficient to achieve correct and computationally efficient solutions for the present study.

6. Conclusions

This paper provides a detailed numerical examination of the flow behaviour and heat transport properties of TeHNF under periodic MHD forces and surface roughness effects. The suggested model, based on a tetra-hybrid nanofluid containing Ag, Au, Cu and TiO_2 nanoparticles distributed in water, exhibits superior thermal performance and offers greater flexibility in altering effective thermophysical parameters than standard mono- and hybrid nanofluids. The results show the synergistic effect of multi-nanoparticle loading, magnetic field modulation and surface roughness on heat transfer and flow control. The main results of this numerical analysis are discussed below:

- The fluid velocity is much higher for the bigger values $\varepsilon \geq 1$ of the wall-velocity parameter than for the lower values $\varepsilon < 1$. This is because of the increased wall speed which has a greater dragging effect on the fluid next to the surface. In this way, the near-wall fluid layers are entrained and accelerated more effectively, which results in improved momentum transfer from the moving wall to the surrounding fluid.
- The sinusoidal oscillations of the $\mathrm{Re}^{1/2}Cf$ are induced by the roughness of the cylindrical surface, which corresponds to the periodic disturbance imposed at the wall. With the increase in Richardson number Ri and ε, the amplitude of these oscillations grows, which indicates that bigger buoyancy effects and stronger surface imperfections aggravate flow fluctuations near the boundary.
- The rough cylindrical surface induces localised protrusions and depressions along the thin geometry, which perturb the near-wall flow and greatly influence the overall flow dynamics.
- The surface roughness of the cylinder wall $\mathrm{Re}^{1/2}Cf$ produces sinusoidal fluctuations in the velocity field. The size of these oscillations grows with increasing surface-roughness amplitude parameter α, which means that the strength of near-wall flow modulation increases with increasing surface undulation.
- The combined impact of the periodic magnetic field and the rough surface is to increase the oscillatory behaviour in $\mathrm{Re}^{-1/2}Nu$ for $\xi > 1$, especially for larger values of the parameters regulating the problem, which indicates a stronger modulation of the flow under coupled magnetic and roughness effects.
- The gradients of velocity and temperature are significantly influenced by the periodic magnetic field compared to the effects of the heat generation and absorption. This is due to the direct effect of the Lorentz force, which drastically alters the momentum flux and the thermal boundary-layer growth.
- The increased influence of the periodic magnetic field results in a more pronounced oscillatory behaviour of the wall heat transfer rate $\mathrm{Re}^{-1/2}Nu$, which is equivalent to a more efficient regulation of the thermal boundary layer by the magnetic field fluctuations.
- The average of the sinusoidal changes in the wall heat-transfer rate slightly improves and rises progressively in the axial direction. Furthermore, higher values of the sphericity parameter s lead to a greater influence on the rate of heat transfer, which signifies a bigger impact of particle shape on thermal transport.
- The highest enhancement values of the Nusselt number for mono, hybrid, ternary and TeHNFs are due to Au nanoparticles (51.92%), hybrid combinations $Au + Cu/H_2O$ (83.00%), ternary nanoparticle mixtures $Au + Cu + TiO_2/H_2O$ (109.69%) and tetra-hybrid compositions of Ag + Au + Cu + TiO2 (104.35%), respectively.
- Mono-nanofluids: Au nanoparticles show the best thermal performance among the mono-nanofluid situations with 51.92% augmentation in the heat-transfer rate.
- The hybrid nanofluids: $Au + Cu/H_2O$ and $Au + TiO_2/H_2O$ exhibit superior thermal performance, achieving heat-transfer enhancements of 83.00% and 72.24%, respectively.
- Ternary-hybrid nanofluids: The ternary nanofluid combinations $Ag + Au + Cu$, $Ag + Au + TiO_2$, $Ag + Cu + TiO_2$ and $Au + Cu + TiO_2$ demonstrate excellent thermal performance, yielding enhanced heat-transfer rates of 78.45%, 79.99%, 80.92% and 109.69%, respectively.
- TeHNF: $Ag + MgO + TiO_2 + Fe_3O_4$ exhibits the highest heat transfer rate at 104.35%.

- Generally, TeHNFs have higher impacts on the velocity and temperature gradients than mono-, hybrid- and ternary nanofluids, indicating their usefulness for improved thermal control system design. However, among all configurations examined, the ternary nanofluid $Au + Cu + TiO_2$ exhibits the highest heat-transfer enhancement, with Ehtr value of 109.69%.

Acknowledgements
The author EM thanks the National Research Foundation of South Africa for their support.

References

Aladdin, N.A.L., Bachok, N. and Pop, I. (2021), "Boundary layer flow and heat transfer of Cu-Al□O□/ water over a moving horizontal slender needle in the presence of hydromagnetic and slip effects", *International Communications in Heat and Mass Transfer*, Vol. 123, p. 105213.

Alghamdi, M., Wakif, A., Thumma, T., Khan, U., Baleanu, D. and Rasool, G. (2021), "Significance of variability in magnetic field strength and heat source on the radiative-convective motion of sodium alginate-based nanofluid within a Darcy-Brinkman porous structure bounded vertically by an irregular slender surface", *Case Studies in Thermal Engineering*, Vol. 28, p. 101428.

Amudhini, M. and De, P. (2024), "Comparative study of hybrid, tri-hybrid, and tetra-hybrid nanoparticles in MHD unsteady flow with chemical reaction, activation energy, Soret-Dufour effect, and sensitivity analysis over non-Darcy porous stretching cylinder". *Heliyon*, Vol. 10 No. 15, p. e35731.

Animasaun, I.L., Shah, N.A., Wakif, A., Mahanthesh, B., Sivaraj, R. and Koríko, O.K. (2022), *Ratio of Momentum Diffusivity to Thermal Diffusivity: Introduction, Meta-Analysis, and Scrutinisation*, Chapman and Hall/CRC, New York, NY.

Chang, L. (1995), "Deterministic modelling and numerical simulation of lubrication between rough surfaces – a review of recent developments", *Wear*, Vol. 184 No. 2, pp. 155–60.

Chen, H., *et al*. (2008), "Rheological behaviour of nanofluids containing TiO_2 nanoparticles", *Journal of Dispersion Science and Technology*, Vol. 29 No. 10, pp. 1412-1417.

Choi, S.U.S. (1995), "Enhancing thermal conductivity of fluids with nanoparticles", *Developments and Applications of Non-Newtonian Flows*, Vol. 66, pp. 99-105.

Farooq, U., Waqas, H., Makki, R., Ali, M.R., Alhushaybari, A., Muhammad, T. and Imran, M. (2023), "Computation of Cattaneo-Christov heat and mass flux model in Williamson nanofluid flow with bioconvection and thermal radiation through a vertical slender cylinder", *Case Studies in Thermal Engineering*, Vol. 42, p. 102736.

Gizewu, T. and Ibrahim, W. (2025), "Stability analysis of Casson tetra-hybrid nanofluid flow", *Journal of Nonlinear Mathematical Physics*, Vol. 32 No. 1, p. 72, available at: link.springer.com

Goud, J.S., Srilatha, P., Kumar, R.V., Kumar, K.T., Khan, U., Raizah, Z., Gill, H.S. and Galal, A.M. (2022), "Role of ternary hybrid nanofluid in the thermal distribution of a dovetail fin with the internal generation of heat", *Case Studies in Thermal Engineering*, Vol. 35, p. 102113.

Grosan, T. and Pop, I. (2011), "Axisymmetric mixed convection boundary layer flow past a vertical cylinder in a nanofluid", *International Journal of Heat and Mass Transfer*, Vol. 54 Nos 15-16, pp. 3139-3145.

Guedri, K., Faridi, A.A., Ahmad, H., Ali, K., Jamshed, W., Abd-Elmonem, A., Abdalla, N.S.E. and Almaliki, A.H. (2025), Thermal analysis of ethylene glycol-based tetra hybrid nanofluid flow over a stretchable permeable surface under the influence of induced magnetic field. *Journal of Molecular Liquids*, p. 128485, doi: 10.1016/j.molliq.2025.128485.

Hussein, U.N., Khashi'ie, N.S., Mukhtar, M.F., Arifin, N.M. and Pop, I. (2025), "Mohd Fariduddin Mukhtar, Norihan Md Arifin, and Ioan Pop, heat transfer optimisation and sensitivity analysis of

ternary hybrid nanofluid flow over a moving surface with joule heating", *J Therm Anal Calorim*, doi: 10.1007/s10973-025-14774-9.

Inouye, K. and Tate, A. (1974), "Finite difference version of quasilinearisation applied to boundary layer equations", *AIAA Journal*, Vol. 12, pp. 558-560.

Jouybari, A.K., Dinarvand, S., Tehrani, P., Yazdi, M.E. and Salehi, G. (2024), "Turbulent flow and heat transfer of Al_2O_3–CuO hybrid nanofluids: comparison of single-phase and multiphase models", *Journal of Nanofluids*, Vol. 13 No. 5, pp. 1134-1144, available at: ingentaconnect.com

Khan, M.I., Waqas, M., Hayat, T., Alsaedi, A. and Khan, M.I. (2017), "Significance of nonlinear radiation in mixed convection flow of magneto Walter-B nanofluid", *Int J Hydrogen Energy*, Vol. 42 No. 42, pp. 26408–26416.

Klazly, M.M. and Bognár, G. (2020), "CFD study for the flow behaviour of nanofluid flow over flat plate", *WSEAS Transactions on Mechanics*, Vol. 14, pp. 49-57, available at: naun.org

Kulkarni, D.P., *et al*. (2006), "Viscosity and rheological behaviour of nanofluids containing oxide nanoparticles", *Colloids and Surfaces A*, Vol. 290 Nos 1-3, pp. 246-250.

Mkhatshwa, M.P., Motsa, S.S., Ayano, M.S. and Sibanda, P. (2020), "MHD mixed convective nanofluid flow about a vertical slender cylinder using overlapping multi-domain spectral collocation approach", *Case Studies in Thermal Engineering*, Vol. 18, p. 100598.

Nabwey, H.A., Armaghani, T., Azizimehr, B., Rashad, A.M. and Chamkha, A.J. (2023), "A comprehensive review of nanofluid heat transfer in porous media", *Nanomaterials*, Vol. 13 No. 5, available at: mdpi.com doi: 10.3390/nano13050937.

Nisha, S.S. and De, P. (2025), "Comparative analysis of di-hybrid, tri-hybrid, tetra-hybrid on bioconvective sisko nanofluid over porous vertical cone/plate with thermal radiation, heat generation, viscous dissipation, and chemical reaction", *Eur. Phys. J. Spec. Top*, doi: 10.1140/epjs/s11734-025-01743-4.

Pak, B.C. and Cho, Y.I. (1998), "Hydrodynamic and heat transfer study of dispersed fluids with submicron metallic oxide particles", *Experimental Heat Transfer*, Vol. 11 No. 2, pp. 151-170, doi: 10.1080/08916159808946559.

Pasaribu, H.R. and Schipper, D.J. (2004), "Deterministic friction model of a rough surface sliding against a flat layered surface", *Tribology Letters*, Vol. 17 No. 4, pp. 967-976.

Patil, P.M., Shashikant, A. and Hiremath, P.S. (2018), "Influence of liquid hydrogen and nitrogen on MHD triple-diffusive mixed convection nano-liquid flow in the presence of surface roughness", *Int J Hydrogen Energy*, Vol. 43 No. 43, pp. 20101-201017.

Patil, P.M. and Benawadi, S. (2024), "Computational study of Casson–Williamson nanoliquid flow over a slender cylinder in the presence of oxytactic microbes: some new insights of inclined magnetic field and surface roughness", *Multiscale and Multidisciplinary Modelling, Experiments and Design*, Vol. 8 No. 7, p. 330.

Patil, P.M. and Benawadi, S. (2022), "Shape effects on the mixed convective hybrid nanoliquid flow over a rough, slender cylinder with convective conditions", *Waves in Random and Complex Media*, Vol. 35 No. 7, pp. 1-17, doi: 10.1080/17455030.2022.2143930.

Patil, P.M. and Kulkarni, M. (2021), "Analysis of MHD mixed convection in a Ag-TiO2 hybrid nanofluid flow past a slender cylinder", *Chinese Journal of Physics*, Vol. 73, pp. 406-419.

Patil, P.M. and Shankar, H.F. (2024), "Analysis of nonlinear thermal radiation and entropy on combined convective ternary (SWCNT-MWCNT-Fe□O□) Eyring-Powell nanoliquid flow over a slender cylinder", *Numerical Heat Transfer, Part A: Applications*, Vol. 85 No. 7, pp. 1042-1062.

Patil, P.M., Benawadi, S., Tonannavar, J.R. and Shanker, B. (2022), "Homogeneous and heterogeneous reactions in the mixed convection flow of hybrid nanofluid over a slender cylinder", *Asia-Pac J Chem Eng*, Vol. 17, p. e2740.

Patil, P.M., Goudar, B. and Momoniat, E. (2024), "Casson-Williamson ternary hybrid nanofluid flow over a yawed cylinder with the impacts of yaw angle and an inclined magnetic field", *International*

Journal of Numerical Methods for Heat and Fluid Flow, Vol. 34 No. 12, pp. 4181-4205, doi: 10.1108/HFF-03-2024-0176.

Patil, P.M., Goudar, B. and Sheremet, M.A. (2025), "Impulsive mixed convection Williamson ternary nanofluid fluid flow about a spinning rough sphere: influence of periodic magnetic effects", *Journal of Thermal Analysis and Calorimetry*, Vol. 150 No. 10, pp. 7887-7899, doi: 10.1007/s10973-025-14173-0.

Patil, P.M., Roy, S. and Pop, I. (2013), "Chemical reaction effects on unsteady mixed convection boundary layer flow past a permeable slender vertical cylinder due to a nonlinearly stretching velocity", *Chemical Engineering Communications*, Vol. 200 No. 3, pp. 398-417, doi: 10.1080/00986445.2011.614978.

Patil, P.M., Shashikant, A. and Hiremath, P.S. (2019), "Effects of surface roughness on mixed convection nanoliquid flow over slender cylinder with liquid hydrogen diffusion", *International Journal of Hydrogen Energy*, Vol. 44 No. 21, pp. 11121-11133.

Paul, P. and Das, S. (2024), "Electro-pumping paradigm of non-Newtonian blood with tetra-hybrid nanoparticles infusion in a ciliated artery", *Chinese Journal of Physics*, Vol. 87, pp. 195-231.

Rashidi, M.M., Nazari, M.A., Mahariq, I., Assad, M.E.H., Ali, M.E., Almuzaiqer, R., Nuhait, A. and Murshid, N. (2021), "Thermophysical properties of hybrid nanofluids and proposed models: a comprehensive review", *Nanomaterials*, Vol. 11 No. 11, p. 3084, available at: mdpi.com doi: 10.3390/nano11113084.

Rehman, A. and Nadeem, S. (2012), "Mixed convection heat transfer in micropolar nanofluid over a vertical slender cylinder", *Chinese Physics Letters*, Vol. 29 No. 12, p. 124701.

Roy, S. and Anilkumar, D. (2006), "Unsteady mixed convection from a moving vertical slender cylinder", *Journal of Heat Transfer*, Vol. 128 No. 4, pp. 368-373, doi: 10.1115/1.2165206.

Safaei, M.R., Jahanbin, A., Kianifar, A., Gharehkhani, S., Kherbeet, A.S., Goodarzi, M. and Dahari, M. (2016), *Mathematical Modeling for Nanofluids Simulation: A Review of the Latest Works*, InTechOpen, available at: cdn.intechopen.com

Samat, N.A.A., Bachok, N. and Arifin, N.M. (2024), "Hybrid carbon nanotubes flow and heat transfer over a vertical thin needle with suction effect: a numerical and optimisation analysis", *International Communications in Heat and Mass Transfer*, Vol. 156, p. 107702.

Schlichting, H. and Gersten, K. (2000), *Boundary Layer Theory*, Springer, New York, NY.

Singh, P.J., Roy, S. and Pop, I. (2008), "Unsteady mixed convection from a rotating vertical slender cylinder in an axial flow", *International Journal of Heat and Mass Transfer*, Vol. 51 Nos 5-6, pp. 1423-1430, doi: 10.1016/j.ijheatmasstransfer.2007.11.024.

Siva Shanker, N., Reddy, M.C.S. and Rao, V.V.B. (2012), "On prediction of viscosity of nanofluids for low volume fractions of nanoparticles", *International Journal of Engineering Research and Technology*, Vol. 1 No. 8, available at: ijert.org

Takhar, H.S., Chamkha, A.J. and Nath, G. (2000), "Combined heat and mass transfer along a vertical moving cylinder with a free stream", *Heat and Mass Transfer*, Vol. 36 No. 3, pp. 237-246, doi: 10.1007/s002310050391.

Tamjid, E. and Guenther, B.H. (2010), "Rheology and colloidal structure of silver nanoparticles dispersed in diethylene glycol", *Powder Technology*, Vol. 197, pp. 49-53.

Timofeeva, E.V., Routbort, J.L. and Singh, D. (2009), "Particle shape effects on thermophysical properties of alumina nanofluids", *Journal of Applied Physics*, Vol. 106 No. 1, p. 014304.

Timofeeva, E.V., Smith, D.S., Yu, W., France, D.M., Singh, D. and Routbort, J.L. (2010), "Particle size and interfacial effects on Thermo-Physical and heat transfer characteristics of Water-Based

α-SiC nanofluids", *Nanotechnology*, Vol. 21 No. 21, p. 215703, doi: 10.1088/0957-4484/21/21/215703.

Trimbitas, R., Grosan, T. and Pop, I. (2011), "Mixed convection boundary layer flow along vertical thin needles in nanofluids", *International Journal of Numerical Methods for Heat and Fluid Flow*, Vol. 24 No. 3, (2014), pp. 579-594.

Varga, R.S. (2000), *Matrix Iterative Analysis*, Prentice-Hall, USA, pp. 219-223.

Waini, I., Ishak, A. and Pop, I. (2019), "Hybrid nanofluid flow and heat transfer past a vertical thin needle with prescribed surface heat flux", *International Journal of Numerical Methods for Heat and Fluid Flow*, Vol. 29 No. 12, pp. 4875-4894.

Corresponding author
Ebrahim Momoniat can be contacted at: emomoniat@uj.ac.za